

HyQuRP: Hybrid quantum-classical neural network with rotational and permutational equivariance for 3D point clouds

Semin Park¹ Chae-Yeun Park^{1,2,3}

Abstract

We introduce HyQuRP, a hybrid quantum-classical neural network equivariant to rotational and permutational symmetries. While existing equivariant quantum machine learning models often rely on ad hoc constructions, HyQuRP is built upon the formal foundations of group representation theory. In the sparse-point regime, HyQuRP consistently outperforms strong classical and quantum baselines across multiple benchmarks. For example, when six subsampled points are used, HyQuRP ($\sim 1.5K$ parameters) achieves 76.13% accuracy on the 5-class ModelNet benchmark, compared to approximately 71% for PointNet, PointMamba, and PointTransformer with similar parameter counts. These results highlight HyQuRP’s exceptional data efficiency and suggest the potential of quantum machine learning models for processing 3D point cloud data.

1. Introduction

Embedding group equivariance into a neural network is one of the most successful principles for designing machine learning models that process data whose features are invariant under group transformations (Cohen & Welling, 2016). A convolutional layer (LeCun et al., 1989; Krizhevsky et al., 2012) is a classic example that preserves translational symmetry in the input, which is relevant for image data whose characteristics are invariant under such transformations. Recently, neural networks equivariant under more advanced symmetries, such as the symmetric group \mathfrak{S}_n (Zaheer et al., 2017; Lee et al., 2019), Euclidean group $E(3)$ (Satorras et al., 2021; Du et al., 2022; Batzner et al., 2022), the special orthogonal group $SO(3)$ (Esteves et al., 2018; Deng et al.,

2021; Kim et al., 2024), and the Lorentz group $SO(1, 3)$ (Bogatskiy et al., 2020; Jahin et al., 2025), have been proposed. These studies report higher classification accuracy and better sample efficiency with fewer parameters across various datasets.

A three-dimensional point cloud, which is a collection of (x, y, z) coordinates representing a surface of objects, inherently has rotational and permutational symmetries, i.e., rotating the entire points by a group transformation $R \in SO(3)$ or permuting the order of points does not change the object it represents. Point clouds are relevant for 3D computer-aided design (CAD) (Wu et al., 2015) and geographic information systems (GIS), and are often obtained from Light Detection and Ranging (LiDAR) (Douillard et al., 2011). An efficient machine learning model for a point cloud dataset may impact autonomous driving, robotics, and geospatial analysis (Guo et al., 2020).

Classical deep learning architectures already achieve strong performance for 3D point clouds on standard benchmarks by explicitly encoding permutational symmetry and incorporating rotation-aware or otherwise geometry-sensitive features, e.g., through point-based convolutions, local neighborhood operators, and invariant pooling layers. In contrast, across a range of standard classification tasks—including 3D point cloud benchmarks—existing quantum machine learning (QML) models have not yet convincingly surpassed such classical baselines. Several empirical studies report that their performance often lags behind well-tuned classical models (Kuros & Kryjak, 2023; Bowles et al., 2024; Schnabel & Roth, 2025), including simple architectures such as MLPs or CNNs, in capacity-controlled comparisons. This persistent gap between classical and quantum models motivates our design of a symmetry-respecting quantum-classical hybrid architecture that can help close this gap and, in the sparse-point regime, outperforms strong classical and quantum baseline models such as PointNet, DGCNN, and RP-EQGNN.

In this paper, we introduce HyQuRP, a hybrid quantum-classical neural network with rotational and permutational equivariance for 3D point clouds. HyQuRP consists of four quantum stages and a classical head, each carefully designed to preserve both the rotation and permutation of input data.

¹School of Integrated Technology, Yonsei University, Seoul 03722, South Korea ²BK21 Graduate Program in Intelligent Semiconductor Technology, Yonsei University, Seoul 03722, South Korea ³Department of Quantum Information, Yonsei University, Seoul 03722, South Korea. Correspondence to: Semin Park <s.park.semin@gmail.com>, Chae-Yeun Park <chae-yeun@yonsei.ac.kr>.

Across several standard 3D point cloud benchmarks under a strictly controlled sparse-point regime (subsampling a few points per object), HyQuRP outperforms classical and quantum state-of-the-art (SOTA) models that are tuned to have similar parameter counts.

The main contributions of this work are summarized as follows:

- We propose HyQuRP, a hybrid quantum-classical architecture that performs classification invariant to global rigid rotations and permutations of the input points.
- We organize all stages of HyQuRP within a unified representation-theoretic framework. In general, quantum circuit architectures that are jointly equivariant under rotational and permutational symmetries are hindered by Schur-Weyl duality. We circumvent this limitation by introducing a minimal per-pair encoding and applying pair-preserving group twirling to construct quantum gates that are equivariant with respect to both rotations and permutations.
- We conduct experiments against strong classical and quantum 3D point cloud baseline models and find that HyQuRP generally surpasses them.

2. Related Work

Equivariant Neural Networks. Equivariant Neural Networks encode known symmetries of the data directly into the architecture, which can improve sample efficiency and generalization. Group-equivariant CNNs generalize standard convolutions from translation equivariance to discrete planar rotations and reflections, improving robustness to rotated 2D images (Cohen & Welling, 2016). For 2D vision, steerable CNNs implement $E(2)$ -equivariant filters that act on feature fields over the plane (Weiler & Cesa, 2019). For 3D geometry, this program has been extended to architectures that are equivariant to $E(3)$, $SO(3)$, or $SE(3)$ using spherical harmonics or tensor features, and applied to spherical signals, 3D point clouds, and atomic systems (Kondor et al., 2018; Esteves et al., 2018; Deng et al., 2021; Gong et al., 2023; Batzner et al., 2022). Similar equivariant architectures have also been developed for $E(n)$ and Lorentz groups (Satorras et al., 2021; Bogatskiy et al., 2020). Across these models, constraining the hypothesis class to respect the underlying symmetry of data typically yields higher accuracy with fewer parameters. Inspired by this principle, HyQuRP is designed to be exactly equivariant to 3D rotations and point permutations for 3D point clouds.

3D Point Cloud Classification Architectures. Deep neural networks for 3D point cloud classification span several architectural families. Point-based families treat point clouds

as unordered sets of 3D coordinates and process them directly with neural networks (Qi et al., 2017a,b; Qian et al., 2022; Ma et al., 2022; Zheng et al., 2023; Zhang et al., 2024). Graph- and relation-based families construct sparse local neighborhoods in coordinate or in feature space, and apply graph convolutions to capture local topology as well as long-range correlations (Wang et al., 2019; Liu et al., 2019; Li et al., 2021; Liu et al., 2022; Tian et al., 2021; Khodadad et al., 2024). More recently, self-attention-based architectures and Mamba-style state-space models have also been adapted for 3D point cloud processing (Zhao et al., 2021; Guo et al., 2021; Yu et al., 2022; Pang et al., 2022; Park et al., 2023; Liang et al., 2024; Han et al., 2024; Wu et al., 2025; Zhang et al., 2025). Beyond these families, other 3D point cloud architectures include projection and multi-view methods, volumetric/voxel CNNs, and surface- or implicit-representation models (Wu et al., 2015; Su et al., 2015; Maturana & Scherer, 2015; Goyal et al., 2021; Ran et al., 2022). Within this taxonomy, HyQuRP falls into the point-based family, as it encodes sets of 3D coordinates and processes them with a quantum-classical hybrid neural network.

Quantum Machine Learning. Quantum machine learning (QML) is an emerging area that combines quantum computing with machine learning. There are various QML models, but one of the most widely studied approaches is parameterized quantum circuits. In this approach, the parameters of a quantum circuit are optimized to solve a given task using gradient-based methods, which directly apply the well-established methodology of classical machine learning.

Earlier research on QML used plain parameterized quantum circuits for solving simple classification tasks (Farhi & Neven, 2018; Mitarai et al., 2018; Schuld et al., 2020). While there have been several claims on the advantages of QML models over classical models even in this simple setup for standard supervised classification tasks (Havlíček et al., 2019; Abbas et al., 2021; Hur et al., 2022), careful comparisons between them generally find that naive quantum models underperform their classical counterparts (Kuros & Kryják, 2023; Bowles et al., 2024; Schnabel & Roth, 2025).

To overcome such a limitation, recent studies have suggested symmetry-imposed QML models (Meyer et al., 2023; Le et al., 2025; Larocca et al., 2022; East et al., 2023; Nguyen et al., 2024). Such symmetries include some simple point groups (Meyer et al., 2023), symmetric groups (Larocca et al., 2022; Nguyen et al., 2024), the $SU(2)$ group (East et al., 2023; Nguyen et al., 2024). Despite such advances, it is not straightforward to design a QML model that is *both* rotation- and permutation-invariant, which is essential for point cloud data. This is because of Schur-Weyl duality, which posits the duality between symmetric group actions and $SU(2)$ rotations on qubits. Thus, a quantum circuit that

is equivariant under the permutation of *any* two qubits and $SU(2)$ group actions must be trivial (see Appendix A.5). HyQuRP avoids this issue by introducing per-pair encoding, which encodes a single 3D point into two qubits, as explained in Section 4.

Thus, papers introducing permutation- and rotation-invariant QML models often rely on additional classical preprocessing. For example, a model introduced in Li et al. (2024) computes the inner products between all pairs of input point vectors, generating $N(N + 1)/2$ input data for the quantum network where N is the number of points in each point set. However, this approach has the following limitations: (1) Since the inner product is invariant under the full orthogonal group $O(3)$ and thus cannot distinguish mirror-reflected point clouds, the model cannot be used for applications where such symmetry is essential, e.g., in molecular structure. (2) The inner product encoding requires $\Theta(N^2)$ total number of qubits. Even for $N \approx 200$, a moderate number for a point cloud dataset, the model requires approximately 20K qubits, which is impractical. By contrast, HyQuRP operates directly on raw coordinates and uses only $2N$ qubits, enabled by a group-theoretic architecture. This design yields a more expressive and practical model than an inner-product-based model.

Most recently, RP-EQGNN was proposed, claiming higher performance than previous QML models on standard 3D point cloud classification benchmarks (Liu et al., 2025). According to the paper, RP-EQGNN exploits rotational and permutational symmetries by parameterizing its equivariant quantum gates using rotation-invariant scalars, such as pairwise distances, angles, and edge types. However, we found that the design described in the paper and the released implementation is insufficient to guarantee permutation- and rotation-invariant outputs (see Appendix C.3). Moreover, RP-EQGNN primarily relies on scalar rotation-invariant features rather than representation-theoretic constructions for quantum dynamics, which may limit its expressivity and generalization compared to HyQuRP. In particular, in our experimental setting, HyQuRP consistently outperforms an RP-EQGNN baseline.

3. Preliminaries

This section reviews mathematical foundations for the design of group-equivariant quantum circuits. We only present several significant results here, while providing a pedagogical review in Appendix A.

3.1. Group Equivariance and Invariance

Let G be a group and let $V : G \rightarrow \text{GL}(X)$ and $W : G \rightarrow \text{GL}(Y)$ be representations of G on X and Y , respectively. A function $f : X \rightarrow Y$ is called G -invariant if $f(V[g] \cdot x) =$

$f(x)$ and G -equivariant if $f(V[g] \cdot x) = W[g] \cdot f(x)$, for all $g \in G$ and $x \in X$.

A common approach to constructing invariant networks is to compose G -equivariant layers with invariant aggregation operations:

$$f_{\text{inv}}(x) = \text{Agg}(f_{\text{eq}}(x)) \quad (1)$$

where f_{eq} preserves group structure and Agg removes it, yielding overall G -invariance.

3.2. $SU(2)$ Equivariant Gates

Single-qubit gates are naturally represented as elements of $SU(2)$, which is a double cover of $SO(3)$. This fundamental relationship allows quantum circuits to be rotation-equivariant in 3D space through the covering map $SU(2) \rightarrow SO(3)$, enabling direct processing of geometric data while preserving rotational symmetries. A crucial observation is that symmetric group elements commute with $SU(2)$ transformations. Formally, a symmetric group element $\sigma \in \mathfrak{S}_n$ transforms a computational basis state $|i_1, i_2, \dots, i_n\rangle$ to

$$\sigma|i_1, i_2, \dots, i_n\rangle = |i_{\sigma^{-1}(1)}, i_{\sigma^{-1}(2)}, \dots, i_{\sigma^{-1}(n)}\rangle \quad (2)$$

Then, for any $U \in SU(2)$, we have $U^{\otimes n}\sigma = \sigma U^{\otimes n}$. This commutation property makes permutations inherently $SU(2)$ -equivariant, providing a foundation for constructing more general equivariant operations.

We extend this concept by introducing a generalized permutation, defined as:

$$\Pi_{\text{general}} = \exp\left[\sum_{\sigma \in \mathfrak{S}_n} c_{\sigma}\sigma\right], \quad (3)$$

where each $c_{\sigma} \in \mathbb{C}$ is a complex coefficient and the sum is over all permutation operators. Since each permutation commutes with $SU(2)$ transformations, the exponential preserves this equivariance property through the series expansion.

Remarkably, this construction is not merely sufficient but also necessary: leveraging Schur's lemma, Schur–Weyl duality, and various tools from representation theory, one can show that every $SU(2)$ -equivariant unitary operator admits such a representation (see Appendix A.6 for details).

3.3. Group Twirling

The twirling formula provides a systematic method for projecting arbitrary operators onto the subspace of group-equivariant operators through group averaging. For a group G acting on a Hilbert space with unitary representation $V[g]$ and operator A , the twirling operation is defined as

$$\mathcal{T}_G[A] = \frac{1}{|G|} \sum_{g \in G} V[g] A V[g]^{\dagger}, \quad (4)$$

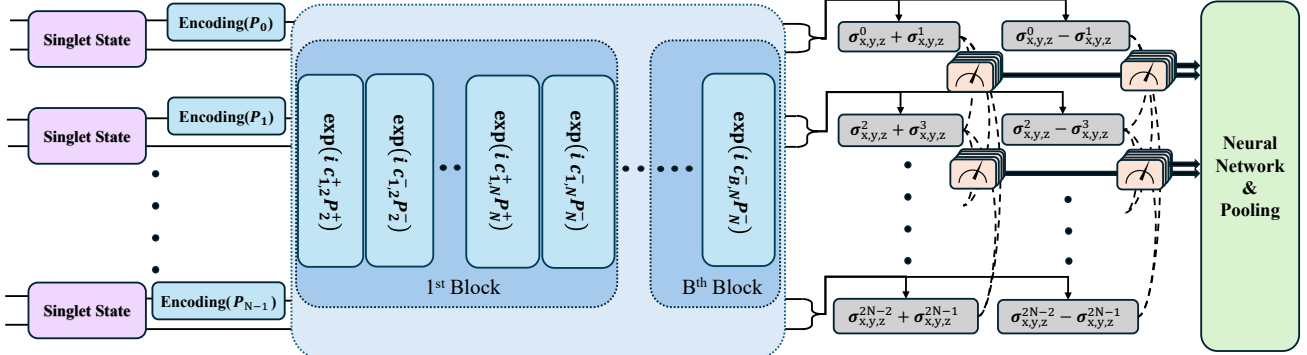


Figure 1. HyQuRP Pipeline. A hybrid pipeline maps a set of N 3D points to a $K \times 1$ score vector, where K is the number of classes. The quantum circuit is constructed as follows: (i) Initialize each qubit pair in the singlet state. (ii) Encode points on the even-indexed qubits ($0, 2, 4, \dots$) while preserving the pair structure. (iii) Apply twirling over cycles of length 2 through N , under appropriate constraints, resulting in two effective gate types for each cycle length; we then repeat this block B times to form a quantum network. (iv) For every unordered pair $\langle i, j \rangle$, measure two types of Hamiltonians ($H_{\langle i,j \rangle}^+$ and $H_{\langle i,j \rangle}^-$), giving a total $2^{\binom{N}{2}}$ expectation values. (v) Send the features to a classical head (pre-pooling neural layers, permutation-invariant pooling, post-pooling classifier) to produce the score vector. Each color indicates how each component behaves under group actions on the input point set: (Purple) rotation- and permutation-invariant, (Blue) rotation- and permutation-equivariant, (Gray) rotation-invariant and permutation-equivariant, (Green) permutation-invariant readout and classifier. Dashed rounded boxes indicate repetition by B .

for a finite group and

$$T_G[A] = \int d\mu(g) V[g] A V[g]^\dagger \quad (5)$$

for a continuous group (compact group) with the normalized Haar measure $\mu(g)$.

By construction, the twirled operators $T_G[A]$ commute with all representation matrices, i.e., commute with $V[g]$ for all $g \in G$, ensuring that they are group equivariant (see Appendix A.7 for a proof). This averaging procedure is fundamental for constructing group-equivariant neural network layers that respect the underlying symmetries of data.

4. Method: HyQuRP

Our framework addresses 3D point cloud classification through a hybrid quantum-classical network that preserves both rotational and permutational symmetries. Given an input point-set (a row of a point cloud dataset) $\mathbf{P} = \{\mathbf{p}_i \in \mathbb{R}^3\}_{i=0}^{N-1}$, our method produces invariant class predictions via the HyQuRP network. Here, N denotes the number of points, and we set the quantum register size to $n = 2N$ qubits (two qubits per point).

As shown in Fig. 1, we decompose HyQuRP into five stages: (i) singlet state initialization, (ii) selective geometric quantum encoding, (iii) a quantum network with rotation and permutation equivariance, (iv) Hamiltonian expectation value measurement, and (v) a classical network. At a high level, stages (i)–(iv) form the quantum backbone and stage (v) is a classical head; together they are mathematically constrained to respect the relevant group actions, so that the overall architecture implements a classifier that is invariant to global

rigid rotations and permutations of the N input points. We describe this construction in the following subsections and provide all additional details and proofs for each component in Appendix B.

4.1. Singlet State Initialization

The quantum processing initiates with the preparation of the n -qubit register in the generalized singlet configuration, implementing the tensor product state

$$|\psi_{\text{initial}}\rangle = \bigotimes_{i=0}^{N-1} \frac{1}{\sqrt{2}} (|01\rangle_{2i,2i+1} - |10\rangle_{2i,2i+1}), \quad (6)$$

where each adjacent qubit pair is the entangled Bell singlet state. This initial state can be easily prepared in a quantum computer, and is $\text{SU}(2)$ invariant as $U \otimes U(|01\rangle - |10\rangle) = |01\rangle - |10\rangle$ for any $U \in \text{SU}(2)$.

4.2. Selective Geometric Quantum Encoding

We encode each 3D point $\mathbf{p} \in \mathbb{R}^3$ using a unitary operator $E(\mathbf{p})$ defined as

$$E(\mathbf{p}) = \exp \left(i \frac{\mathbf{p} \cdot \vec{\sigma}}{\Theta} \right), \quad (7)$$

where $\vec{\sigma} = \{X, Y, Z\}$ is a vector of Pauli operators and Θ is a fixed hyperparameter introduced to improve numerical stability. By construction, $E(\mathbf{p})$ depends on the vector \mathbf{p} and is equivariant to 3D rotations: For any $R \in \text{SO}(3)$ with corresponding $U_R \in \text{SU}(2)$,

$$E(R\mathbf{p}) = U_R E(\mathbf{p}) U_R^\dagger, \quad (8)$$

from the standard $SU(2)$ – $SO(3)$ correspondence.

Our n -qubit singlet initialization is only invariant under pair-preserving permutations (not arbitrary permutations of the n individual qubits). Accordingly, we adopt a per-pair selective encoding where only the even-indexed qubits in each pair $(2j, 2j+1)$ are geometrically encoded. This encoding preserves the pair-wise structure and makes the overall encoding pairwise permutation-equivariant. Because any nontrivial pure states are not simultaneously invariant under global $SU(2)$ rotations and all permutations of the qubits, it is impossible to use all qubits for encoding while preserving both symmetries. Consequently, our selective per-pair scheme is a minimal and effective design (see Appendix B.2 for details).

4.3. Quantum Network with Rotation and Permutation Equivariance

Building upon the $SU(2)$ –equivariant operators established in Section 3.2, we now construct our quantum circuit architecture that achieves dual equivariance under both rotations and permutations. While the generalized permutation operators are $SU(2)$ –equivariant, they do not by themselves enforce the permutation symmetry inherent in set-valued point cloud representations.

To construct symmetric group-equivariant gates while preserving the pair-wise structure, we twirl over the subgroup of \mathfrak{S}_n that permutes the singlet pairs as rigid blocks. We group wire indices into disjoint pairs:

$$B_\ell := \{2\ell, 2\ell+1\}, \quad \ell = 0, \dots, N-1. \quad (9)$$

Then, we define the pair-permuting subgroup

$$\mathfrak{S}_{\text{pair}} := \{\sigma : \{B_\ell\} \rightarrow \{B_\ell\} | \sigma \text{ is bijective}\} \leq \mathfrak{S}_{2N}, \quad (10)$$

which acts by permuting these pairs as whole blocks while leaving the internal structure of each pair intact. Because $\mathfrak{S}_{\text{pair}}$ never mixes the two wires inside a pair, we are free to choose the relative sign on the non-encoding partner wire in each pair. Accordingly, we distinguish two cases, positive and negative, and perform the twirl separately for each sign.

For each $k \in \{2, \dots, N\}$ and the set of pairs

$$\mathcal{P} = \{(0, 1), (2, 3), \dots, (n-2, n-1)\}, \quad (11)$$

let $\text{Perm}(\mathcal{P}, k)$ be the set of ordered k -tuples (p_1, \dots, p_k) of distinct elements, where each $p_m = (2j_m, 2j_m+1) \in \mathcal{P}$. Given a k -tuple of pairs $\pi \in \text{Perm}(\mathcal{P}, k)$ and a selection vector $\mathbf{s} = (s_1, \dots, s_k) \in \{0, 1\}^k$, we define $\tau_\pi^{\mathbf{s}}$ to be the permutation matrix that acts as the k -cycle

$$(2j_1 + s_1, 2j_2 + s_2, \dots, 2j_k + s_k), \quad (12)$$

on the selected wires and leaves all other wires fixed.

We define

$$P_k^+ := \frac{1}{k!} \sum_{\pi \in \text{Perm}(\mathcal{P}, k)} \sum_{\mathbf{s} \in \{0, 1\}^k} \tau_\pi^{\mathbf{s}}, \quad (13)$$

$$P_k^- := \frac{1}{k!} \sum_{\pi \in \text{Perm}(\mathcal{P}, k)} \sum_{\mathbf{s} \in \{0, 1\}^k} (-1)^{\|\mathbf{s}\|_1} \tau_\pi^{\mathbf{s}}, \quad (14)$$

where $\|\mathbf{s}\|_1 = \sum_{\ell=1}^k s_\ell$ is the Hamming weight of \mathbf{s} . The operators P_k^{\pm} are Hermitian and commute with the pair-permuting action of S_{pair} . These operators are specifically constructed to be invariant under pair-permutations, but symmetric or anti-symmetric under the internal permutation, i.e., swap the qubits within each pair. However, this is not the only possible outcome of the twirling; see Appendix B.3 for further details.

Our dual-equivariant gate combines these matrices over all k values:

$$G^l = \prod_{k=2}^N e^{ic_{l,k}^+ P_k^+} e^{ic_{l,k}^- P_k^-}, \quad (15)$$

and our quantum circuit is just a stack of B blocks G^ℓ , given as

$$C = \prod_{l=1}^B G^l, \quad (16)$$

where $c_{l,k}^{\pm}$ are the trainable parameters for block ℓ and cycle length k .

This construction yields a gate that is equivariant with respect to both the global $SU(2)$ rotation and the pair-preserving permutation actions, allowing pointwise representations under these groups to flow consistently between adjacent components and thereby acting as a symmetry-preserving bridge within the network.

4.4. Hamiltonian Expectation Value Measurement

The final quantum processing stage computes expectation values using pairwise Heisenberg Hamiltonians:

$$H_{\langle i,j \rangle}^+ = \sum_{\alpha \in \{X, Y, Z\}} (\sigma_\alpha^{2i} + \sigma_\alpha^{2i+1}) \otimes (\sigma_\alpha^{2j} + \sigma_\alpha^{2j+1}), \quad (17)$$

$$H_{\langle i,j \rangle}^- = \sum_{\alpha \in \{X, Y, Z\}} (\sigma_\alpha^{2i} - \sigma_\alpha^{2i+1}) \otimes (\sigma_\alpha^{2j} - \sigma_\alpha^{2j+1}), \quad (18)$$

where σ_α^q denotes the Pauli- α operator acting on q -th qubit. Because both the initialization and encoding operate on fixed singlet pairs $(2i, 2i+1)$, permutation-equivariant operators must also act at the pair level, which consist of factors in the form of $(\sigma_\alpha^{2i} \pm \sigma_\alpha^{2i+1})$.

Moreover, we want $SU(2)$ -invariant Hamiltonians at the operator level, in the sense that applying any global $SU(2)$

rotation acts on H by conjugation and leaves it unchanged. Thus, we have $H_{\langle i,j \rangle}^{\pm}$, which are of Heisenberg form, as the lowest-order Hamiltonians that are invariant under rigid rotations of the input. Since i and j run over all distinct sites, and we have the sign choice (\pm) , the total number of measurement outcomes is $2^{\binom{N}{2}}$.

However, the measurement outcomes exhibit permutation equivariance rather than invariance—when points are permuted, the corresponding expectation values undergo the same permutation. This equivariance property requires subsequent permutation-invariant classical processing steps to convert the quantum measurements into rotation- and permutation-invariant class predictions.

4.5. Classical Network

After the quantum stages, we process two types of Hamiltonian expectation values $\mathbf{x} \in \mathbb{R}^{\binom{N}{2} \times 2}$ with a classical head, which is invariant under permutations. Our classical head, which we refer to as Set-MLP, has a structure similar to DeepSets (Zaheer et al., 2017) and consists of two MLP blocks separated by a symmetric aggregation function. The first MLP block is applied to the last dimension, resulting in $\mathbf{y} \in \mathbb{R}^{\binom{N}{2} \times d}$. We then apply a symmetric aggregation function f to \mathbf{y} over the Hamiltonian index:

$$\mathbf{y}_{\text{agg}} = f(\mathbf{y}), \quad f \in \{\text{mean, max, min, sum, var, std}\},$$

yielding $\mathbf{y}_{\text{agg}} \in \mathbb{R}^{6d}$. The aggregated representation is then passed through the second MLP block to output class logits, trained with cross-entropy.

4.6. Group Equivariance of Overall Architecture

Combining all components, our complete quantum-classical framework achieves both rotational and permutational invariance through distinct mechanisms operating at different stages of the pipeline.

Our framework achieves rotation invariance through the quantum processing pipeline. When a 3D rotation $R \in \text{SO}(3)$ is applied to the input point cloud, let $U_R \in \text{SU}(2)$ denotes the corresponding global rotation on the n -qubit Hilbert space. Then, we first see that the encoding layer $\mathcal{E} = \bigotimes_{i=0}^{N-1} E(\mathbf{p}_i) \otimes I_2$ transforms as

$$\mathcal{E} \mapsto \mathcal{E}' = \bigotimes_{i=0}^{N-1} E(R\mathbf{p}_i) \otimes I_2 \quad (19)$$

$$= \bigotimes_{i=0}^{N-1} U_R E(\mathbf{p}_i) U_R^\dagger \otimes I_2 = U_R^{\otimes n} \mathcal{E}(U_R^\dagger)^{\otimes n} \quad (20)$$

Accordingly, the transformation of the expectation value is

given as:

$$\begin{aligned} & \langle \psi_{\text{output}} | H | \psi_{\text{output}} \rangle_{\text{rotation}} \\ &= \langle \psi_0 | \mathcal{E}'^\dagger C^\dagger H C \mathcal{E}' | \psi_0 \rangle \\ &= \langle \psi_0 | U_R^{\otimes 2N} \mathcal{E}^\dagger C^\dagger (U_R^\dagger)^{\otimes 2N} H U_R^{\otimes 2N} C \mathcal{E} (U_R^\dagger)^{\otimes 2N} | \psi_0 \rangle \\ &= \langle \psi_0 | \mathcal{E}^\dagger C^\dagger H C \mathcal{E} | \psi_0 \rangle \\ &= \langle \psi_{\text{output}} | H | \psi_{\text{output}} \rangle_{\text{origin}}, \end{aligned} \quad (21)$$

where C is our $\text{SU}(2)$ -equivariant quantum circuit that satisfies $U^{\otimes 2N} C = C U^{\otimes 2N}$ for all single-qubit unitary operator $U \in \text{SU}(2)$ and $|\psi_0\rangle$ denotes a series of N singlet states. The singlet state is inherently rotation invariant, remaining unchanged under $\text{SU}(2)$ transformations. The equivariant gates naturally commute with rotations, allowing the rotation operators U_R and U_R^\dagger to propagate through to the Hamiltonian. Since our Heisenberg Hamiltonians are $\text{SU}(2)$ -invariant, the $\text{SU}(2)$ operators cancel out, demonstrating that the quantum expectation values remain unchanged under arbitrary 3D rotations of the input point cloud.

For permutation invariance, our framework operates through a two-stage process. The quantum processing stage is permutation-equivariant end-to-end, so it propagates symmetric, pointwise representations up to the classical head. When the input points undergo an index permutation Π , the Hamiltonian expectation value, computed in the same manner as above, is given by:

$$\Pi \left(\langle \psi_{\text{output}} | H_{\langle i,j \rangle}^{\pm} | \psi_{\text{output}} \rangle_{\text{origin}} \right) \quad (22)$$

$$= \langle \psi_{\text{output}} | H_{\langle \Pi(i), \Pi(j) \rangle}^{\pm} | \psi_{\text{output}} \rangle_{\Pi}, \quad (23)$$

The classical neural network then passes the measurements through MLP blocks and a statistical pooling operation, which is inherently invariant to input permutations.

This two-stage approach—quantum equivariance followed by classical invariance—ensures that the final classification predictions remain unchanged regardless of the ordering of input points.

By enforcing permutation and rotation invariance at the architectural level, our framework enables more robust and data-efficient 3D point cloud classification. This symmetry guarantee is grounded in the representation-theoretic interplay between quantum dynamics and the group structures of rotations and permutations, which we leverage to design quantum gates and classical readouts that preserve these invariants end-to-end.

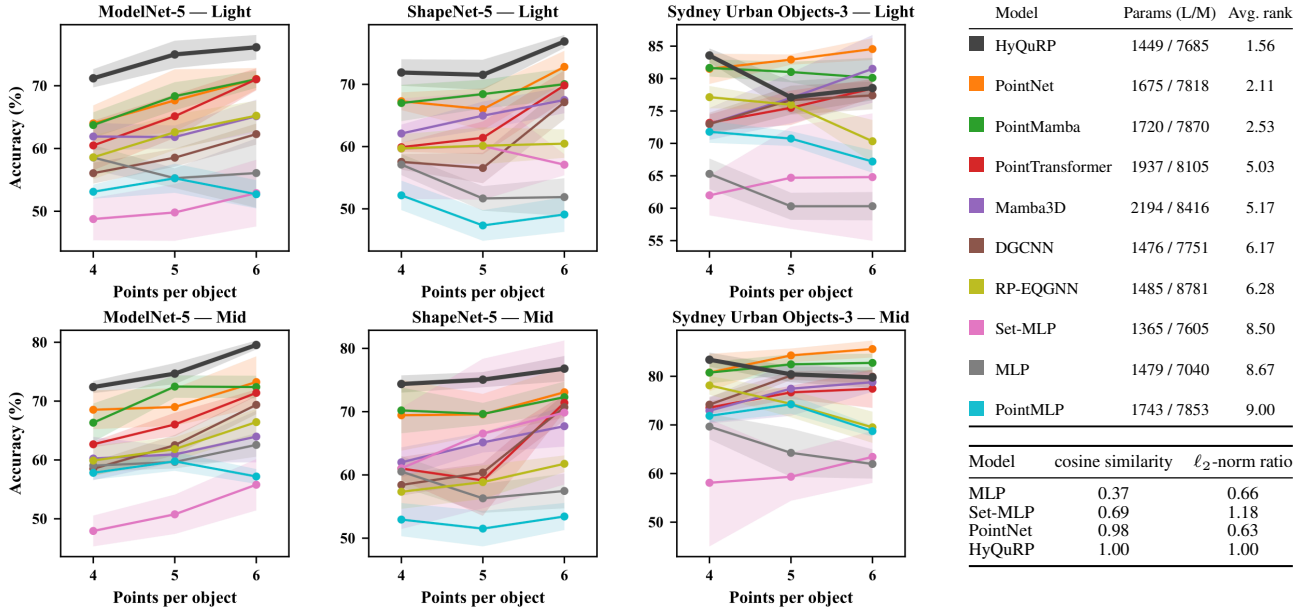


Figure 2. Overall Results. Solid curves represent the mean accuracy across all seeds (per dataset and point budget) and shaded regions indicate $\pm\sigma$. The upper-right table reports trainable parameter counts (Light/Mid) and the average ranks aggregated over all settings (lower is better). The lower-right table reports cosine similarity and ℓ_2 -norm ratio between the logits produced from a single point-set and its rotated and permuted counterparts after 10 epochs; definitions and details are provided in Appendix D.

5. Experiments

In this section, we evaluate point cloud classification under our experimental setting, comparing HyQuRP against various quantum and classical baseline models. The main results are summarized in Fig. 2 and Tab. 1. Our code is available in github.com/YonseiQC/equivariant_QML.

5.1. Experimental setup

We use our small-class subsets: ModelNet-5, ShapeNet-5, and Sydney Urban Objects-3, where the suffix denotes the number of classes we selected from each dataset. ModelNet (Wu et al., 2015) is a widely used collection of clean CAD meshes of man-made objects; ShapeNetCore (Chang et al., 2015) is a large-scale repository of 3D CAD models with a unified taxonomy and substantial intra-class geometric variation; Sydney Urban Objects (De Deuge et al., 2013) contains object-level LiDAR point clouds from urban driving with real-world sparsity, occlusions, and sensor noise. We enforce object-level disjointness between the test and the training/validation sets and subsample points via farthest-point sampling (FPS) from shapes centered at the origin (zero-mean) and scaled to unit maximum radius (i.e., $\max_i \|\mathbf{x}_i\|_2 = 1$). We use a small number of subsampled points, $N \in \{4, 5, 6\}$, which allows the corresponding quantum circuits to be simulated on classical computers within a reasonable time. In training, these subsampled points are augmented by applying three types of random transformations: SO(3) rotation, permutation, and jitter.

Training uses Adam (batch size 35) for 1,000 epochs; for each model, the same learning rate η is used for all datasets and $N \in \{4, 5, 6\}$, which is optimized for the ModelNet-5 dataset with $N = 4$ over $\eta \in \{10^{-2}, 10^{-3}, 10^{-4}\}$. We do not use a learning rate scheduler, weight decay, dropout, EMA, or early stopping. All results are reported as mean \pm std of test top-1 accuracy over 7 seeds; for each seed, the checkpoint with the highest validation accuracy is evaluated on the test set. Details of the dataset design and construction are provided in Appendix C.1; implementation and experimental environments are in Appendix C.2.

5.2. Baselines

Our goal in the sparse-point regime is to compare architectural designs under matched capacity. Canonical point cloud classification models are typically instantiated with 1024–2048 input points and tens of output classes (e.g., ModelNet40), resulting in multi-million-parameter models. In contrast, our setting operates on only a small number of points per object and classes, so directly reusing those standard configurations would introduce far more parameters per point than the data can support, obscuring the effect of the architectural design rather than the raw capacity. We therefore define two parameter budgets, Light ($\sim 1.5K$ parameters) and Mid ($\sim 7K$), and instantiate both our HyQuRP models and all baselines at these levels so that performance differences primarily reflect architectural choices rather than raw capacity.

Dataset	HyQuRP	PointNet	PointMamba	PointTransformer	Mamba3D	DGCNN	RP-EQGNN	Set-MLP	MLP	PointMLP
MN-5	76.13 / 79.54	71.09 / 73.24	71.03 / 72.40	71.03 / 71.40	65.14 / 63.97	62.29 / 69.37	65.23 / 66.43	52.89 / 55.79	56.09 / 62.56	52.71 / 57.19
SN-5	76.89 / 76.80	72.81 / 73.07	70.03 / 72.30	69.83 / 71.41	67.49 / 67.70	67.13 / 70.71	60.47 / 61.76	57.09 / 69.86	51.89 / 57.46	49.09 / 53.43
SUO-3	78.53 / 79.76	84.55 / 85.61	80.11 / 82.76	78.47 / 77.44	81.50 / 78.79	77.40 / 79.93	70.33 / 69.51	64.80 / 63.43	60.31 / 61.97	67.20 / 68.73

Table 1. Test accuracy (%) at 6 points across datasets. Each entry reports the mean test accuracy over 7 seeds for two capacity-matched variants (Light/Mid). MN-5, SN-5, and SUO-3 denote ModelNet-5, ShapeNet-5, and Sydney Urban Objects-3, respectively.

Within this capacity-matched setting, we compare the HyQuRP against the following model families: a plain MLP, Set-MLP (our classical ablation: quantum modules removed, classical pipeline unchanged), PointNet (Qi et al., 2017a), DGCNN (Wang et al., 2019), PointMLP (Ma et al., 2022), PointTransformer (Zhao et al., 2021), PointMamba (Liang et al., 2024), Mamba3D (Han et al., 2024) and RP-EQGNN (Liu et al., 2025). For each baseline, we preserve its canonical building blocks and heads while systematically reducing depth/width until it fits the Light/Mid budgets. Internal resampling layers are also dropped, since they would reduce the point set too aggressively under our point budget. In neighborhood-based models, we form small local groups by choosing a small k (the number of nearest neighbors) commensurate with N .

We refer to Appendix C.3 for full architectural details of the baselines, including the original designs and our implementation differences.

5.3. Results and Analysis

As shown in Fig. 2, across all three datasets and both Light ($\sim 1.5K$ parameters) and Mid ($\sim 7K$) regimes, HyQuRP achieves the best overall average rank (1.56). In particular, HyQuRP consistently outperforms the baselines in CAD-style datasets (ModelNet, ShapeNet). More precisely, on ModelNet with 6 points (Light), HyQuRP achieves 76.13% test accuracy, exceeding the top-performing baselines—PointNet (71.09%), PointMamba (71.03%), and PointTransformer (71.03%)—by +5.04, +5.10, and +5.10 percentage points, respectively (Tab. 1). The same pattern holds on ShapeNet and in the Mid setting. On the LiDAR-style SUO dataset, HyQuRP remains one of the strongest methods in both the Light and Mid regimes, albeit less dominant compared to CAD-style datasets. Overall, these results indicate a substantial improvement over a diverse set of strong baselines across datasets and model sizes, under our experimental protocol.

In our experimental setting, on ModelNet with 6 points (Light), Set-MLP (our permutation-invariant classical head) achieves 52.89% test accuracy, which is 23.24 percentage points lower than HyQuRP (Tab. 1). On average over all settings, HyQuRP outperforms Set-MLP by 18.09 ± 6.18 percentage points, even though the primary difference is the quantum component with ~ 100 parameters. Set-MLP

is not rotation-invariant, whereas HyQuRP is rotation- and permutation-invariant (Fig. 2); this invariance property can contribute to the observed gap. Moreover, HyQuRP’s quantum blocks operate in a 2^n -dimensional Hilbert space for n qubits, which may offer additional expressivity that is not reflected by the small parameter increase.

6. Conclusion and Discussion

We introduced HyQuRP, a quantum-classical hybrid machine learning model with rotation and permutation equivariance to enable group-invariant 3D point cloud classification. Our design is based on group representation theory, ensuring both theoretical depth and structural elegance. Across standard 3D point cloud benchmarks with a small number of classes and points, HyQuRP generally outperforms state-of-the-art baselines (Fig. 2, Tab. 1). These gains are primarily driven by the quantum part, indicating the potential of quantum-enhanced representations in this regime.

In this work, we simulated quantum circuits classically, which do not scale to large qubit counts, thereby limiting our evaluation to small point sets and precluding dense point clouds. While current quantum devices are also too noisy to run our algorithm, with a fault-tolerant quantum computer that might be available in a decade or two, our equivariant gates can be implemented using, e.g., Suzuki-Trotter product (Childs et al., 2021), linear combination of unitaries (Childs & Wiebe, 2012; Berry et al., 2015), and quantum singular value transformation (Gilyén et al., 2019).

Our experiments conducted here avoided commonly used techniques such as data re-uploading, resampling, and neighborhood grouping, as they may break the mathematical symmetries. Moreover, for simplicity, we only utilized a limited set of quantum gates by imposing additional mathematical constraints, leaving room for further performance improvements. We hope our work offers a new perspective on quantum machine learning and encourages further research in this direction.

Impact Statement

This paper presents work whose goal is to advance the field of Machine Learning. There are many potential societal consequences of our work, none of which we feel must be specifically highlighted here.

References

Abbas, A., Sutter, D., Zoufal, C., Lucchi, A., Figalli, A., and Woerner, S. The power of quantum neural networks. *Nature Computational Science*, 1(6):403–409, 6 2021. doi: 10.1038/s43588-021-00084-1.

Batzner, S., Musaelian, A., Sun, L., Geiger, M., Mailoa, J. P., Kornbluth, M., Molinari, N., Smidt, T. E., and Kozinsky, B. E(3)-equivariant graph neural networks for data-efficient and accurate interatomic potentials. *Nature communications*, 13(1):2453, 2022.

Berry, D. W., Childs, A. M., Cleve, R., Kothari, R., and Somma, R. D. Simulating hamiltonian dynamics with a truncated taylor series. *Physical review letters*, 114(9):090502, 2015.

Bogatskiy, A., Anderson, B., Offermann, J., Roussi, M., Miller, D., and Kondor, R. Lorentz group equivariant neural network for particle physics. In *International Conference on Machine Learning*, pp. 992–1002. PMLR, 2020.

Bowles, J., Ahmed, S., and Schuld, M. Better than classical? the subtle art of benchmarking quantum machine learning models. *arXiv preprint arXiv:2403.07059*, 2024.

Chang, A. X., Funkhouser, T., Guibas, L., Hanrahan, P., Huang, Q., Li, Z., Savarese, S., Savva, M., Song, S., Su, H., Xiao, J., Yi, L., and Yu, F. Shapenet: An information-rich 3D model repository. *arXiv preprint arXiv:1512.03012*, 2015.

Childs, A. M. and Wiebe, N. Hamiltonian simulation using linear combinations of unitary operations. *arXiv preprint arXiv:1202.5822*, 2012.

Childs, A. M., Su, Y., Tran, M. C., Wiebe, N., and Zhu, S. Theory of trotter error with commutator scaling. *Physical Review X*, 11(1):011020, 2021.

Cohen, T. and Welling, M. Group equivariant convolutional networks. In *International conference on machine learning*, pp. 2990–2999. PMLR, 2016.

De Deuge, M., Quadros, A., Hung, C., and Douillard, B. Unsupervised feature learning for classification of outdoor 3D scans. In *Australasian conference on robotics and automation*, volume 2, pp. 1. University of New South Wales Kensington, Australia, 2013.

Deng, C., Litany, O., Duan, Y., Poulenard, A., Tagliasacchi, A., and Guibas, L. J. Vector neurons: A general framework for SO(3)-equivariant networks. In *Proceedings of the IEEE/CVF International Conference on Computer Vision*, pp. 12200–12209, 2021.

Douillard, B., Underwood, J., Kuntz, N., Vlaskine, V., Quadros, A., Morton, P., and Frenkel, A. On the segmentation of 3D LIDAR point clouds. In *2011 IEEE International Conference on Robotics and Automation*, pp. 2798–2805. IEEE, 2011.

Du, W., Zhang, H., Du, Y., Meng, Q., Chen, W., Zheng, N., Shao, B., and Liu, T.-Y. SE(3) equivariant graph neural networks with complete local frames. In *International Conference on Machine Learning*, pp. 5583–5608. PMLR, 2022.

East, R. D. P., Alonso-Linaje, G., and Park, C.-Y. All you need is spin: SU(2) equivariant variational quantum circuits based on spin networks. *arXiv preprint arXiv:2309.07250*, 2023.

Esteves, C., Allen-Blanchette, C., Makadia, A., and Daniilidis, K. Learning SO(3) equivariant representations with spherical cnns. In *Proceedings of the european conference on computer vision (ECCV)*, pp. 52–68, 2018.

Farhi, E. and Neven, H. Classification with quantum neural networks on near term processors. 2018. doi: 10.48550/arXiv.1802.06002.

Gilyén, A., Su, Y., Low, G. H., and Wiebe, N. Quantum singular value transformation and beyond: exponential improvements for quantum matrix arithmetics. In *Proceedings of the 51st annual ACM SIGACT symposium on theory of computing*, pp. 193–204, 2019.

Gong, X., Li, H., Zou, N., Xu, R., Duan, W., and Xu, Y. General framework for E(3)-equivariant neural network representation of density functional theory hamiltonian. *Nature Communications*, 14(1):2848, 2023.

Goyal, A., Law, H., Liu, B., Newell, A., and Deng, J. Revisiting point cloud shape classification with a simple and effective baseline. In *Proceedings of the 38th International Conference on Machine Learning (ICML)*, pp. 3809–3820, 2021.

Guo, M.-H., Cai, J.-X., Liu, Z.-N., Mu, T.-J., Martin, R. R., and Hu, S.-M. Pct: Point cloud transformer. *Computational Visual Media*, 7(2):187–199, 2021. doi: 10.1007/s41095-021-0229-5.

Guo, Y., Wang, H., Hu, Q., Liu, H., Liu, L., and Bennamoun, M. Deep learning for 3D point clouds: A survey. *IEEE transactions on pattern analysis and machine intelligence*, 43(12):4338–4364, 2020.

Han, X., Tang, Y., Wang, Z., and Li, X. Mamba3D: Enhancing local features for 3D point cloud analysis via state space model. In *Proceedings of the 2024 ACM Multimedia Conference (ACM MM)*, 2024.

Havlíček, V., Córcoles, A. D., Temme, K., Harrow, A. W., Kandala, A., Chow, J. M., and Gambetta, J. M. Supervised learning with quantum-enhanced feature spaces. *Nature*, 567(7747):209–212, 3 2019. doi: 10.1038/s41586-019-0980-2.

Hur, T., Kim, L., and Park, D. K. Quantum convolutional neural network for classical data classification. *Quantum Machine Intelligence*, 4(1):3, 2022.

Jahin, M. A., Masud, M. A., Suva, M. W., Mridha, M. F., and Dey, N. Lorentz-equivariant quantum graph neural network for high-energy physics. *IEEE Transactions on Artificial Intelligence*, 2025.

Khodadad, M., Shiraei Kasmaee, A., Mahyar, H., and Rezanejad, M. Mlgcn: An ultra efficient graph convolutional neural model for 3D point cloud analysis. *Frontiers in Artificial Intelligence*, 7:1439340, 2024. doi: 10.3389/frai.2024.1439340.

Kim, J., Yoo, H. B., Han, D.-S., Song, Y.-J., and Zhang, B.-T. Continuous $SO(3)$ equivariant convolution for 3D point cloud analysis. In *European Conference on Computer Vision*, pp. 59–75. Springer, 2024.

Kondor, R., Lin, Z., and Trivedi, S. Clebsch–Gordan nets: a fully fourier space spherical convolutional neural network. *Advances in Neural Information Processing Systems*, 31, 2018.

Krizhevsky, A., Sutskever, I., and Hinton, G. E. Imagenet classification with deep convolutional neural networks. *Advances in neural information processing systems*, 25, 2012.

Kuros, S. and Kryjak, T. Traffic sign classification using deep and quantum neural networks. In *Computer Vision and Graphics*, Lecture Notes in Networks and Systems, pp. 43–55. Springer, 2023. doi: 10.1007/978-3-031-22025-8_4.

Larocca, M., Sauvage, F., Sbahi, F. M., Verdon, G., Coles, P. J., and Cerezo, M. Group-invariant quantum machine learning. *PRX quantum*, 3(3):030341, 2022.

Le, I. N. M., Kiss, O., Schuhmacher, J., Tavernelli, I., and Tacchino, F. Symmetry-invariant quantum machine learning force fields. *New Journal of Physics*, 27(2):023015, 2025.

LeCun, Y., Boser, B., Denker, J. S., Henderson, D., Howard, R. E., Hubbard, W., and Jackel, L. D. Backpropagation applied to handwritten zip code recognition. *Neural computation*, 1(4):541–551, 1989.

Lee, J., Lee, Y., Kim, J., Kosiorek, A., Choi, S., and Teh, Y. W. Set transformer: A framework for attention-based permutation-invariant neural networks. In *International conference on machine learning*, pp. 3744–3753. PMLR, 2019.

Li, Y., Chen, H., Cui, Z., Timofte, R., Pollefeys, M., Van Gool, L., and Chirikjian, G. S. Towards efficient graph convolutional networks for point cloud handling. In *Proceedings of the IEEE/CVF International Conference on Computer Vision (ICCV)*, pp. 3752–3762, 2021.

Li, Z., Nagano, L., and Terashi, K. Enforcing exact permutation and rotational symmetries in the application of quantum neural network on point cloud datasets. *Physical Review Research*, 6:043028, 2024. doi: 10.1103/PhysRevResearch.6.043028.

Liang, D., Zhou, X., Xu, W., Zhu, X., Zou, Z., Ye, X., Tan, X., and Bai, X. PointMamba: A simple state space model for point cloud analysis. In *Advances in Neural Information Processing Systems (NeurIPS)*, 2024. arXiv:2402.10739.

Liu, S., Liu, D., Chen, C., and Xu, C. SGCNN for 3D point cloud classification. In *Proceedings of the 2022 14th International Conference on Machine Learning and Computing (ICMLC)*, pp. 419–423, 2022.

Liu, W., Zhu, Y., Zha, Y., Wu, Q., Jian, L., and Liu, Z. Rotation- and permutation-equivariant quantum graph neural network for 3D graph data. *IEEE Transactions on Pattern Analysis and Machine Intelligence*, 47(11):10329–10343, 2025. doi: 10.1109/TPAMI.2025.3593371.

Liu, Y., Fan, B., Xiang, S., and Pan, C. Relation-shape convolutional neural network for point cloud analysis. In *Proceedings of the IEEE/CVF Conference on Computer Vision and Pattern Recognition (CVPR)*, pp. 8895–8904, 2019.

Ma, X., Qin, C., You, S., Ran, X., Fu, Y., Wang, C., Qiao, Y., Yuille, A., Zhou, B., and Gao, Y. Rethinking network design and local geometry in point clouds: A simple mlp-based architecture. In *Proc. ICLR*, 2022. PointMLP.

Maturana, D. and Scherer, S. Voxnet: A 3D convolutional neural network for real-time object recognition. In *Proceedings of the IEEE/RSJ International Conference on Intelligent Robots and Systems (IROS)*, pp. 922–928, 2015.

Meyer, J. J., Mularski, M., Gil-Fuster, E., Mele, A. A., Arzani, F., Wilms, A., and Eisert, J. Exploiting symmetry in variational quantum machine learning. *PRX quantum*, 4(1):010328, 2023.

Mitarai, K., Negoro, M., Kitagawa, M., and Fujii, K. Quantum circuit learning. *Physical Review A*, 98:032309, 2018. doi: 10.1103/PhysRevA.98.032309.

Nguyen, Q. T., Schatzki, L., Braccia, P., Ragone, M., Coles, P. J., Sauvage, F., Larocca, M., and Cerezo, M. Theory for equivariant quantum neural networks. *PRX Quantum*, 5(2):020328, 2024.

Pang, Y., Wang, W., Tay, F. E. H., Liu, W., Tian, Y., and Yuan, L. Masked autoencoders for point cloud self-supervised learning. In *Proceedings of the European Conference on Computer Vision (ECCV)*, 2022.

Park, J., Lee, S., Kim, S., Xiong, Y., and Kim, H. J. Self-positioning point-based transformer for point cloud understanding. In *Proceedings of the IEEE/CVF Conference on Computer Vision and Pattern Recognition (CVPR)*, pp. 21814–21823, 2023. doi: 10.1109/CVPR52729.2023.02089.

Qi, C. R., Su, H., Mo, K., and Guibas, L. J. Pointnet: Deep learning on point sets for 3D classification and segmentation. In *Proceedings of the IEEE conference on computer vision and pattern recognition*, pp. 652–660, 2017a.

Qi, C. R., Yi, L., Su, H., and Guibas, L. J. Pointnet++: Deep hierarchical feature learning on point sets in a metric space. In *Advances in Neural Information Processing Systems (NeurIPS)*, volume 30, 2017b.

Qian, G., Li, Y., Peng, H., Mai, J., Hammoud, H. A. A. K., Elhoseiny, M., and Ghanem, B. Pointnext: Revisiting pointnet++ with improved training and scaling strategies. *Advances in Neural Information Processing Systems*, 35: 23192–23204, 2022.

Ran, H., Liu, J., and Wang, C. Surface representation for point clouds. In *Proceedings of the IEEE/CVF Conference on Computer Vision and Pattern Recognition (CVPR)*, 2022.

Satorras, V. G., Hoogeboom, E., and Welling, M. E(n) equivariant graph neural networks. In *International conference on machine learning*, pp. 9323–9332. PMLR, 2021.

Schnabel, J. and Roth, M. Quantum kernel methods under scrutiny: a benchmarking study. *Quantum Machine Intelligence*, 7(1):58, 2025. doi: 10.1007/s42484-025-00273-5.

Schuld, M., Bocharov, A., Svore, K., and Wiebe, N. Circuit-centric quantum classifiers. *Physical Review A*, 101: 032308, 2020. doi: 10.1103/PhysRevA.101.032308.

Su, H., Maji, S., Kalogerakis, E., and Learned-Miller, E. Multi-view convolutional neural networks for 3D shape recognition. In *Proceedings of the IEEE International Conference on Computer Vision (ICCV)*, pp. 945–953, 2015.

Tian, Y., Chen, L., Song, W., Sung, Y., and Woo, S. Dgcbnet: Dynamic graph convolutional broad network for 3D object recognition in point cloud. *Remote Sensing*, 13(1): 66, 2021. doi: 10.3390/rs13010066.

Wang, Y., Sun, Y., Liu, Z., Sarma, S. E., Bronstein, M. M., and Solomon, J. M. Dynamic graph cnn for learning on point clouds. *ACM Transactions on Graphics*, 38(5): 1–12, 2019.

Weiler, M. and Cesa, G. General E(2)-equivariant steerable CNNs. *Advances in neural information processing systems*, 32, 2019.

Wu, P., Chai, B., Li, H., Zheng, M., Peng, Y., Wang, Z., Nie, X., Zhang, Y., and Sun, X. Spiking point transformer for point cloud classification. In *Proceedings of the AAAI Conference on Artificial Intelligence*, 2025.

Wu, Z., Song, S., Khosla, A., Yu, F., Zhang, L., Tang, X., and Xiao, J. 3D ShapeNets: A deep representation for volumetric shapes. In *Proceedings of the IEEE Conference on Computer Vision and Pattern Recognition (CVPR)*, pp. 1912–1920, 2015.

Yu, X., Tang, L., Rao, Y., Huang, T., Zhou, J., and Lu, J. Point-bert: Pre-training 3D point cloud transformers with masked point modeling. In *Proceedings of the IEEE/CVF Conference on Computer Vision and Pattern Recognition (CVPR)*, 2022.

Zaheer, M., Kottur, S., Ravanbakhsh, S., Poczos, B., Salakhutdinov, R. R., and Smola, A. J. Deep sets. *Advances in neural information processing systems*, 30, 2017.

Zhang, T., Yuan, H., Qi, L., Zhang, J., Zhou, Q., Ji, S., Yan, S., and Li, X. Point cloud mamba: Point cloud learning via state space model. In *Proceedings of the AAAI Conference on Artificial Intelligence*, volume 39, pp. 10121–10130, 2025.

Zhang, Z., Lin, L., and Zhi, X. R-pointnet: Robust 3D object recognition network for real-world point clouds corruption. *Applied Sciences*, 14(9):3649, 2024. doi: 10.3390/app14093649.

Zhao, H., Jiang, L., Jia, J., Torr, P. H. S., and Koltun, V. Point transformer. In *Proc. ICCV*, pp. 16259–16268, 2021.

Zheng, S., Pan, J., Lu, C., and Gupta, G. Pointnorm: Dual normalization is all you need for point cloud analysis. In *Proceedings of the International Joint Conference on Neural Networks (IJCNN)*, 2023. arXiv:2207.06324.

A. Group Theory

A.1. Basics of Group Theory

Group Definition. A group (G, \cdot) is a set G equipped with a binary operation $\cdot : G \times G \rightarrow G$ satisfying the following axioms: (i) associativity: $(a \cdot b) \cdot c = a \cdot (b \cdot c)$ for all $a, b, c \in G$; (ii) existence of identity element: there exists $e \in G$ such that $e \cdot a = a \cdot e = a$ for all $a \in G$; (iii) existence of inverse: for each $a \in G$, there exists $a^{-1} \in G$ such that $a \cdot a^{-1} = a^{-1} \cdot a = e$.

Group homomorphism. A map $\varphi : G \rightarrow H$ is a group homomorphism if $\varphi(g_1 g_2) = \varphi(g_1) \varphi(g_2)$ for all $g_1, g_2 \in G$. Its kernel and image are $\ker \varphi = \{g \in G : \varphi(g) = e_H\}$ and $\text{im } \varphi = \varphi(G)$, where e_G and e_H denote the identity elements of G and H . The map φ is injective if and only if $\ker \varphi = \{e_G\}$, and it is surjective if and only if $\text{im } \varphi = H$. We denote a set of all homomorphisms to itself, $\iota : G \rightarrow G$, by $\text{End}(G)$. A bijective homomorphism is an isomorphism. If there exists an isomorphism between G and H , we write $G \cong H$. An automorphism is an isomorphism $\alpha : G \rightarrow G$; the set of all automorphisms, $\text{Aut}(G)$, forms a group under composition.

Group representation. A (linear) representation of a group G on a vector space V over a field \mathbb{K} is a homomorphism $\rho : G \rightarrow \text{GL}(V)$. Here $\text{GL}(V)$ denotes the group of all invertible linear maps $V \rightarrow V$ under composition; if $\dim_{\mathbb{K}} V = d$, then, for a given basis of V , $\text{GL}(V) \cong \text{GL}_d(\mathbb{K})$. We write $\rho(g)v$ for the action of $g \in G$ on $v \in V$, which satisfies $\rho(e) = \text{Id}_V$ and $\rho(g_1 g_2) = \rho(g_1) \rho(g_2)$. In Hilbert spaces one often uses a unitary representation $\rho : G \rightarrow \mathcal{U}(\mathcal{H})$ where $\mathcal{U}(\mathcal{H})$ is the unitary group on \mathcal{H} .

Irreducible representation. Let $\rho : G \rightarrow \text{GL}(V)$ be a representation. A subspace $W \subset V$ is G -invariant if $\rho(g)W \subseteq W$ for all $g \in G$. The representation ρ is called irreducible if it has no nontrivial G -invariant subspace, i.e., the only G -invariant subspaces are $\{0\}$ and V ; otherwise it is reducible.

Lie algebra. A Lie algebra \mathfrak{g} is (typically) realized as the tangent space at the identity of a Lie group G , equipped with a bilinear bracket. Concretely, for a Lie group G the Lie algebra is

$$\mathfrak{g} := T_e G = \{\dot{\gamma}(0) : \gamma : (-\varepsilon, \varepsilon) \rightarrow G \text{ smooth, } \gamma(0) = e\}, \quad (24)$$

together with a bilinear map $[\cdot, \cdot] : \mathfrak{g} \times \mathfrak{g} \rightarrow \mathfrak{g}$ (the Lie bracket) that is antisymmetric and satisfies the Jacobi identity

$$[X, Y] = -[Y, X], \quad [X, [Y, Z]] + [Y, [Z, X]] + [Z, [X, Y]] = 0. \quad (25)$$

For a matrix Lie group $G \subseteq \text{GL}_n(\mathbb{C})$, one can identify

$$\mathfrak{g} = \{X \in \mathbb{C}^{n \times n} : \exp(tX) \in G \text{ for all sufficiently small } t\}, \quad (26)$$

and in this case the Lie bracket is simply the matrix commutator

$$[X, Y] := XY - YX. \quad (27)$$

A.2. SU(2) Group

SU(2) Group Definition. $\text{SU}(2) = \{U \in \mathbb{C}^{2 \times 2} : U^\dagger U = I, \det(U) = 1\}$, with group operation given by matrix multiplication (identity I , inverse $U^{-1} = U^\dagger$). Every $U \in \text{SU}(2)$ can be written as

$$U = \begin{pmatrix} \alpha & -\bar{\beta} \\ \beta & \bar{\alpha} \end{pmatrix}, \quad \alpha, \beta \in \mathbb{C}, \quad |\alpha|^2 + |\beta|^2 = 1. \quad (28)$$

The Lie algebra of $\text{SU}(2)$ is given by

$$\mathfrak{su}(2) = \{A \in \mathbb{C}^{2 \times 2} : A^\dagger = -A, \text{tr } A = 0\}, \quad (29)$$

spanned (over \mathbb{R}) by $\{i\sigma_x, i\sigma_y, i\sigma_z\}$, where the Pauli matrices are

$$\sigma_x = \begin{pmatrix} 0 & 1 \\ 1 & 0 \end{pmatrix}, \quad \sigma_y = \begin{pmatrix} 0 & -i \\ i & 0 \end{pmatrix}, \quad \sigma_z = \begin{pmatrix} 1 & 0 \\ 0 & -1 \end{pmatrix}. \quad (30)$$

They satisfy

$$[\sigma_i, \sigma_j] = 2i \epsilon_{ijk} \sigma_k. \quad (31)$$

Equivalently, any Lie-algebra element $X \in \mathfrak{su}(2)$ can be written as

$$X = -\frac{i}{2} \theta \hat{n} \cdot \vec{\sigma}, \quad (32)$$

and exponentiating yields a group element $\exp(X) \in \mathrm{SU}(2)$.

Connection to 3D rotation.

$$\Phi : \mathrm{SU}(2) \rightarrow \mathrm{SO}(3) \text{ is surjective with kernel } \{\pm I\}, \quad \mathrm{SO}(3) \cong \mathrm{SU}(2)/\{\pm I\}. \quad (33)$$

Proof. The space of traceless Hermitian 2×2 matrices is a vector space over \mathbb{R} with a basis $\{\sigma_x, \sigma_y, \sigma_z\}$. For $U \in \mathrm{SU}(2)$ and each j , unitary conjugation preserves the hermiticity and trace, so

$$U \sigma_j U^\dagger = \sum_{i=1}^3 R_{ij}(U) \sigma_i, \quad (34)$$

for $R_{ij}(U) \in \mathbb{R}$. Then, we define Φ as

$$\Phi(U) = (R_{ij}(U))_{1 \leq i, j \leq 3}. \quad (35)$$

One can show that Φ satisfies the desired properties as follows.

First, multiplying by σ_k and taking the trace of both sides of Eq. (34) gives

$$\mathrm{tr}(\sigma_k U \sigma_j U^\dagger) = \sum_i R_{ij}(U) \mathrm{tr}(\sigma_k \sigma_i). \quad (36)$$

Hence, we obtain

$$R_{kj}(U) = \frac{1}{2} \mathrm{tr}(\sigma_k U \sigma_j U^\dagger) \quad (\because \mathrm{tr}(\sigma_k \sigma_i) = 2\delta_{ki}). \quad (37)$$

We then prove that $R_{ij}(U) \in \mathrm{SO}(3)$ by evaluating $\frac{1}{2} \mathrm{tr}(U \sigma_i U^\dagger U \sigma_j U^\dagger)$ in two ways. First,

$$\frac{1}{2} \mathrm{tr}(U \sigma_i U^\dagger U \sigma_j U^\dagger) = \frac{1}{2} \mathrm{tr}(\sigma_i \sigma_j) = \delta_{ij} \quad (38)$$

Second, expanding $U \sigma_i U^\dagger$ and $U \sigma_j U^\dagger$ in the Pauli basis via (34), we rewrite the left-hand side in terms of $R(U)$:

$$\begin{aligned} \frac{1}{2} \mathrm{tr}(U \sigma_i U^\dagger U \sigma_j U^\dagger) &= \frac{1}{2} \mathrm{tr}\left(\left(\sum_{k=1}^3 R_{ki}(U) \sigma_k\right) \left(\sum_{\ell=1}^3 R_{\ell j}(U) \sigma_\ell\right)\right) \\ &= \sum_{k, \ell} R_{ki}(U) R_{\ell j}(U) \frac{1}{2} \mathrm{tr}(\sigma_k \sigma_\ell) \\ &= \sum_k R_{ki}(U) R_{kj}(U) = (R(U)^\top R(U))_{ij}. \end{aligned} \quad (39)$$

Comparing the two expressions yields $(R(U)^\top R(U))_{ij} = \delta_{ij}$, i.e., $R(U)^\top R(U) = I$. Moreover, by continuity and $R(I) = I$, we get $\det(R(U)) = +1$, hence $R(U) \in \mathrm{SO}(3)$.

Next, we prove that Φ is a homomorphism. By the linearity, for any $\vec{v} \in \mathbb{R}^3$,

$$U(\vec{v} \cdot \vec{\sigma}) U^\dagger = \sum_{i, j} R_{ij}(U) v_j \sigma_i = (R(U) \vec{v}) \cdot \vec{\sigma}. \quad (40)$$

Thus the assignment $\Phi : \mathrm{SU}(2) \rightarrow \mathrm{SO}(3)$, $U \mapsto R(U)$, is well-defined and satisfies

$$(UV)(\vec{v} \cdot \vec{\sigma})(UV)^\dagger = U(V(\vec{v} \cdot \vec{\sigma})V^\dagger)U^\dagger \Rightarrow \Phi(UV) = \Phi(U)\Phi(V), \quad (41)$$

(i.e., a group homomorphism).

If $\Phi(U) = I$, then $U\sigma_i U^\dagger = \sigma_i$ for all i , hence U commutes with the matrix algebra generated by $\{\sigma_i\}$ and must be $\pm I$; therefore $\ker \Phi = \{\pm I\}$. Moreover, the differential $d\Phi_e : \mathfrak{su}(2) \rightarrow \mathfrak{so}(3)$ is an isomorphism, so the image is the connected Lie subgroup with Lie algebra $\mathfrak{so}(3)$, namely $\mathrm{SO}(3)$, hence $\mathrm{im}(\Phi) = \mathrm{SO}(3)$. Since $\mathrm{im}(\Phi) = \mathrm{SO}(3)$ and $\ker \Phi = \{\pm I\}$, the First Isomorphism Theorem yields $\mathrm{SO}(3) \cong \mathrm{SU}(2)/\{\pm I\}$.

Single-qubit gates. Single-qubit operations can be represented by $\mathrm{SU}(2)$. Standard rotations

$$R_x(\theta) = e^{-i\theta\sigma_x/2}, \quad R_y(\theta) = e^{-i\theta\sigma_y/2}, \quad R_z(\theta) = e^{-i\theta\sigma_z/2} \quad (42)$$

generate arbitrary $U \in \mathrm{SU}(2)$ (e.g., ZYZ/Euler decompositions).

SU(2) irreducible representations. All finite-dimensional unitary irreps of $\mathrm{SU}(2)$ are indexed by total angular momentum $j \in \{0, \frac{1}{2}, 1, \frac{3}{2}, \dots\}$. The spin- j irrep $V^{(j)}$ has dimension $2j+1$ with weight basis $\{|j, m\rangle : m = -j, -j+1, \dots, j\}$ on which the generators J_x, J_y, J_z satisfy $[J_x, J_y] = iJ_z$ (cyclic), $J_z|j, m\rangle = m|j, m\rangle$, $J^2|j, m\rangle = j(j+1)|j, m\rangle$, and with $J_\pm := J_x \pm iJ_y$,

$$J_\pm|j, m\rangle = \sqrt{(j \mp m)(j \pm m + 1)}|j, m \pm 1\rangle. \quad (43)$$

Group elements $U = \exp(-i\theta \hat{n} \cdot \vec{\sigma}/2)$ act in spin- j as $D^{(j)}(U) = \exp(-i\theta \hat{n} \cdot \mathbf{J}^{(j)})$, with $\mathbf{J}^{(1/2)} = \frac{1}{2}\vec{\sigma}$. Tensor products decompose by the Clebsch–Gordan rule $V^{(j_1)} \otimes V^{(j_2)} = \bigoplus_{j=|j_1-j_2|}^{j_1+j_2} V^{(j)}$; in particular

$$V^{(1/2)} \otimes V^{(1/2)} = V^{(0)} \oplus V^{(1)}, \quad (44)$$

where the one-dimensional $j = 0$ block is the singlet. For simplicity, one often uses j to denote $V^{(j)}$, e.g., $1/2 \otimes 1/2 = 0 \oplus 1$.

A.3. Symmetric Group

Let $[n] := \{1, \dots, n\}$ and define the symmetric group as the set of all set–set bijections

$$\mathfrak{S}_n \equiv \mathrm{Sym}([n]) := \{\sigma : [n] \rightarrow [n] \mid \sigma \text{ bijective}\}. \quad (45)$$

With composition $(\sigma, \sigma') \mapsto \sigma \circ \sigma'$, identity $\mathrm{id}_{[n]}$, and inverses σ^{-1} , we have $|\mathfrak{S}_n| = n!$. Every $\sigma \in \mathfrak{S}_n$ admits a decomposition into disjoint cycles, unique up to ordering; the cycle type (a partition $\lambda \vdash n$) determines the conjugacy class.

On the n -qubit space $(\mathbb{C}^2)^{\otimes n}$ we use the action that permutes tensor factors. Define

$$\Pi : \mathfrak{S}_n \longrightarrow \mathrm{U}((\mathbb{C}^2)^{\otimes n}), \quad \Pi(\sigma)(v_1 \otimes \dots \otimes v_n) := v_{\sigma^{-1}(1)} \otimes \dots \otimes v_{\sigma^{-1}(n)}. \quad (46)$$

On computational basis states $|x_1 \dots x_n\rangle$ with $x_i \in \{0, 1\}$,

$$\Pi(\sigma)|x_1 \dots x_n\rangle = |x_{\sigma^{-1}(1)} \dots x_{\sigma^{-1}(n)}\rangle. \quad (47)$$

The inverse of indices ensures homomorphism:

$$\Pi(\sigma)\Pi(\sigma') = \Pi(\sigma\sigma'), \quad \Pi(\mathrm{id}) = I. \quad (48)$$

A.4. Schur's Lemma

Statement & Proof. Let $\rho : G \rightarrow GL(V)$ and $\sigma : G \rightarrow GL(W)$ be irreducible G -representations over a field K , and let $T : V \rightarrow W$ be a linear map such that $\sigma(g)T = T\rho(g)$ for all $g \in G$ (i.e., T is a G -intertwiner). Then:

1. Either $T = 0$ or T is an isomorphism $V \xrightarrow{\cong} W$.
2. In particular, if $V = W$ and $\rho = \sigma$ over an algebraically closed field, then $T = \lambda I_V$ for some $\lambda \in K$.

Proof. Because T intertwines the actions, both $\ker T \subseteq V$ and $\mathrm{Im} T \subseteq W$ are G -invariant: For any $v \in \ker T$ and $g \in G$, $T(\rho(g)v) = \sigma(g)T(v) = 0$, hence $\rho(g)v \in \ker T$. For any $u \in \mathrm{Im} T$, choose $v' \in V$ with $u = T(v')$; then $\sigma(g)u = \sigma(g)T(v') = T(\rho(g)v') \in \mathrm{Im} T$. Irreducibility gives $\ker T \in \{0, V\}$ and $\mathrm{Im} T \in \{0, W\}$. If $T \neq 0$, then $\mathrm{Im} T = W$ and $\ker T = 0$, hence T is bijective. Over an algebraically closed field, any $T \in \mathrm{End}_G(V)$ has an eigenvalue λ ; then $T - \lambda I$ is an intertwiner with nontrivial kernel, so it must be zero, yielding $T = \lambda I$.

Schur's Lemma Application in $SU(2)$. View n qubits as n copies of the spin- $\frac{1}{2}$ irrep of $SU(2)$. The tensor space decomposes as

$$(\mathbb{C}^2)^{\otimes n} \cong \bigoplus_J \mathbb{C}^{m_J} \otimes \mathcal{H}_J. \quad (49)$$

where \mathcal{H}_J is the spin- J irrep and m_J is its multiplicity. The Schur (spin) map S_n implements this change of basis, sending the computational basis to the spin basis in which the $SU(2)$ action is block diagonal by total spin J .

Let U be any $SU(2)$ -equivariant linear operator on $(\mathbb{C}^2)^{\otimes n}$ (equivalently, U commutes with the group action). Conjugating into the spin basis, let $U_{J,J'}$ be a block of U between spin- J and spin- J' space, i.e., $U_{J,J'} : \mathbb{C}^{m_{J'}} \otimes \mathcal{H}_{J'} \rightarrow \mathbb{C}^{m_J} \otimes \mathcal{H}_J$. The commutation relation reads

$$(I_{m_J} \otimes \rho_J(g)) U_{J,J'} = U_{J,J'} (I_{m_{J'}} \otimes \rho_{J'}(g)), \quad \forall g \in SU(2), \quad (50)$$

where $\rho_J : SU(2) \rightarrow \text{U}(\mathcal{H}_J)$ denotes the spin- J irrep. Each $U_{J,J'}$ is therefore an intertwiner between irreps. By Schur's Lemma, $U_{J,J'} = 0$ unless $J = J'$, so U is block diagonal in the spin basis; moreover, on each irrep block,

$$U|_{\mathbb{C}^{m_J} \otimes \mathcal{H}_J} = A_J \otimes I_{\mathcal{H}_J}, \quad A_J \in \text{End}(\mathbb{C}^{m_J}), \quad (51)$$

Thus, after transforming by \mathfrak{S}_n , every $SU(2)$ -equivariant operator decomposes as $\bigoplus_J (A_J \otimes I_{\mathcal{H}_J})$: It acts as the identity on each spin irrep \mathcal{H}_J , with freedom only on the multiplicity spaces.

A.5. Schur–Weyl Duality

Statement & Proof Let $V \cong \mathbb{C}^d$ and $W := V^{\otimes n}$. There are commuting actions

$$\rho : GL(V) \rightarrow GL(W), \quad \rho(g) = g^{\otimes n}, \quad \Pi : \mathfrak{S}_n \rightarrow GL(W), \quad \Pi(\sigma) \text{ permutes tensor factors}, \quad (52)$$

so that $\rho(g)\Pi(\sigma) = \Pi(\sigma)\rho(g)$ for all $g \in GL(V), \sigma \in \mathfrak{S}_n$. Write

$$\mathcal{A} := \Pi(\mathbb{C}[\mathfrak{S}_n]) \subseteq \text{End}(W), \quad \mathcal{B} := \text{alg}\langle g^{\otimes n} : g \in GL(V) \rangle \subseteq \text{End}(W). \quad (53)$$

Then

$$\mathcal{A} = \text{End}_{GL(V)}(W), \quad \mathcal{B} = \text{End}_{\mathbb{C}[\mathfrak{S}_n]}(W). \quad (54)$$

Moreover, there is a canonical simultaneous decomposition

$$W \cong \bigoplus_{\lambda \vdash n, \ell(\lambda) \leq d} S_\lambda(V) \otimes \mathfrak{S}^\lambda, \quad (55)$$

where \mathfrak{S}^λ is the Specht module (irreducible \mathfrak{S}_n -module) and $S_\lambda(V)$ is the Schur functor applied to V (irreducible $GL(V)$ -module). The sum is over all λ , the shape of a Young tableau with n boxes, and $\ell(\lambda)$ is the number of rows in the Young tableau with shape λ . We require $\ell(\lambda) \leq d$, which is the necessary and sufficient condition for $S_\lambda(V) \neq 0$.

Proof. Since ρ and Π commute, $\mathcal{A} \subseteq \text{End}_{GL(V)}(W)$ and $\mathcal{B} \subseteq \text{End}_{\mathbb{C}[\mathfrak{S}_n]}(W)$. Over \mathbb{C} , W is semisimple for the commuting algebras \mathcal{A} and \mathcal{B} . By the double centralizer theorem, the inclusions are equalities and W decomposes as a direct sum of tensor products of irreducibles:

$$W \cong \bigoplus_{\lambda} S_\lambda(V) \otimes \mathfrak{S}^\lambda. \quad (56)$$

In the following paragraph, we characterize $\mathfrak{S}_\lambda(V)$ inside W using Young symmetrizers.

How to construct the block $S_\lambda(V) \otimes \mathfrak{S}^\lambda$ Fix a partition $\lambda \vdash n$ and a Young tableau T of shape λ . Let $R_T \leq \mathfrak{S}_n$ be the row stabilizer and $C_T \leq \mathfrak{S}_n$ the column stabilizer. Define

$$a_T = \sum_{\sigma \in R_T} \sigma, \quad b_T = \sum_{\tau \in C_T} \text{sgn}(\tau) \tau, \quad e_T = a_T b_T \in \mathbb{C}[\mathfrak{S}_n]. \quad (57)$$

In general $e_T^2 = c_T e_T$ for some nonzero scalar c_T ; set the *primitive idempotent* $e_T^\circ := c_T^{-1} e_T$ so that $(e_T^\circ)^2 = e_T^\circ$. Then

$$\mathfrak{S}^\lambda \cong \mathbb{C}[\mathfrak{S}_n] \cdot e_T^\circ, \quad S_\lambda(V) \cong \Pi(e_T^\circ) W. \quad (58)$$

Choosing a different T of the same shape gives an isomorphic module.

A linear basis of \mathfrak{S}^λ is given by *polytabloids* attached to the standard Young tableaux (SYT) of shape λ : if $\{T\}$ denotes the tabloid of T , the basis vectors are

$$E_T := e_T^\circ \{T\}. \quad (59)$$

A linear basis of $S_\lambda(V)$ is indexed by *semi-standard Young tableaux* (SSYT) of shape λ filled with $\{1, \dots, d\}$: rows weakly increasing and columns strictly increasing. Writing $V = \mathbb{C}^d$ with basis $\{e_1, \dots, e_d\}$ and listing the SSYT entries as (t_1, \dots, t_n) in box order, the corresponding basis vectors are

$$v_t := \Pi(e_T^\circ)(e_{t_1} \otimes e_{t_2} \otimes \dots \otimes e_{t_n}). \quad (60)$$

(Here T is any fixed tableau of shape λ ; different choices produce canonically isomorphic bases.)

Dimensions For $\lambda \vdash n$ with boxes u , hook length $h(u)$ and content $c(u) = \text{col}(u) - \text{row}(u)$,

$$\dim \mathfrak{S}^\lambda = \frac{n!}{\prod_{u \in \lambda} h(u)}, \quad \dim S_\lambda(\mathbb{C}^d) = \prod_{u \in \lambda} \frac{d + c(u)}{h(u)}. \quad (61)$$

Schur–Weyl Duality Application in $\text{SU}(2)$. Specialize to $V = \mathbb{C}^2$ and restrict $\rho(g) = g^{\otimes n}$ from $GL(2)$ to the subgroup $\text{SU}(2)$, acting by global rotations $U^{\otimes n}$. Then only partitions with at most two rows appear:

$$(\mathbb{C}^2)^{\otimes n} \cong \bigoplus_{\lambda \vdash n, \ell(\lambda) \leq 2} S_\lambda(\mathbb{C}^2) \otimes \mathfrak{S}^\lambda. \quad (62)$$

Equivalently, one may index the decomposition by total spin $J \in \{\frac{n}{2}, \frac{n}{2} - 1, \dots\}$ via $\lambda(J) = (\frac{n}{2} + J, \frac{n}{2} - J)$, where $S_{\lambda(J)}(\mathbb{C}^2)$ is the spin- J irrep of $\text{SU}(2)$.

Let A be an operator on n -qubit Hilbert space $(\mathbb{C}^2)^{\otimes n}$ that satisfies

$$[A, U^{\otimes n}] = 0 \quad \forall U \in \text{SU}(2), \quad [A, \Pi(\sigma)] = 0 \quad \forall \sigma \in \mathfrak{S}_n. \quad (63)$$

Under the Schur–Weyl decomposition, A is forced to be a scalar on each λ -block:

$$A = \bigoplus_{\lambda \vdash n, \ell(\lambda) \leq 2} c_\lambda I_{S_\lambda(\mathbb{C}^2)} \otimes I_{\mathfrak{S}^\lambda}, \quad c_\lambda \in \mathbb{C}. \quad (64)$$

In particular, if A is unitary then $c_\lambda = e^{i\theta_\lambda}$ and A can only apply a phase on each total-spin sector.

Proof. Since $[A, U^{\otimes n}] = 0$, A lies in $\text{End}_{\text{SU}(2)}((\mathbb{C}^2)^{\otimes n})$, which equals the image of $\mathbb{C}[\mathfrak{S}_n]$ by Schur–Weyl duality. Thus, on each summand $S_\lambda(\mathbb{C}^2) \otimes \mathfrak{S}^\lambda$, Schur’s Lemma implies that $A|_\lambda = I_{S_\lambda(\mathbb{C}^2)} \otimes B_\lambda$ for some $B_\lambda \in \text{End}(\mathfrak{S}^\lambda)$. Similarly, $[A, \Pi(\sigma)] = 0$ forces $A|_\lambda = C_\lambda \otimes I_{\mathfrak{S}^\lambda}$ for some $C_\lambda \in \text{End}(S_\lambda(\mathbb{C}^2))$. Therefore $A|_\lambda = c_\lambda I \otimes I$ on each block.

A.6. $\text{SU}(2)$ Equivariant Gate and Generalized Permutation

SU(2) Equivariant Gate to Generalized Permutation. Let $W = (\mathbb{C}^2)^{\otimes n}$ be a vector space with $\text{SU}(2)$ -action $\rho(U) = U^{\otimes n}$ and the permutation action $\Pi(\sigma)$ of $\sigma \in \mathfrak{S}_n$. Then

$$\text{End}_{\text{SU}(2)}(W) = \Pi(\mathbb{C}[\mathfrak{S}_n]), \quad (65)$$

i.e., every operator commuting with $\rho(U)$ lies in the group algebra generated by $\{\Pi(\sigma)\}_{\sigma \in \mathfrak{S}_n}$. In particular, any operator of the form

$$Q = \exp\left(\sum_{j=1}^m c_j \Pi(\sigma_j)\right), \quad c_j \in \mathbb{C}, \sigma_j \in \mathfrak{S}_n, \quad (66)$$

is $\text{SU}(2)$ -equivariant.

Proof. Recall that \mathfrak{S}_n acts on W by permuting tensor factors via

$$\Pi(\sigma)(|v_1\rangle \otimes \dots \otimes |v_n\rangle) = |v_{\sigma^{-1}(1)}\rangle \otimes \dots \otimes |v_{\sigma^{-1}(n)}\rangle. \quad (67)$$

Moreover, the diagonal $SU(2)$ -action $\rho(U) = U^{\otimes n}$ commutes with this permutation action:

$$\rho(U) \Pi(\sigma) = \Pi(\sigma) \rho(U), \quad \forall U \in SU(2), \sigma \in \mathfrak{S}_n. \quad (68)$$

By Schur–Weyl duality specialized to $d = 2$,

$$W \cong \bigoplus_{\lambda \vdash n, \ell(\lambda) \leq 2} S_\lambda(V) \otimes \mathfrak{S}^\lambda, \quad (69)$$

where $S_\lambda(V)$ are the $SU(2)$ irreps (total spin blocks) and \mathfrak{S}^λ are the Specht modules of \mathfrak{S}_n . With respect to this decomposition the $SU(2)$ -commutant is

$$\text{End}_{SU(2)}(W) = \Pi(\mathbb{C}[\mathfrak{S}_n]) \cong \bigoplus_{\lambda} \mathbf{1}_{S_\lambda(V)} \otimes \text{End}(\mathfrak{S}^\lambda), \quad (70)$$

i.e., operators commuting with all $\rho(U)$ act trivially on $S_\lambda(V)$ and arbitrarily on the multiplicity spaces \mathfrak{S}^λ .

We call

$$Q := \exp\left(\sum_{j=1}^m c_j \Pi(\sigma_j)\right), \quad c_j \in \mathbb{C}, \sigma_j \in \mathfrak{S}_n, \quad (71)$$

a *generalized permutation*. Since $\Pi(\mathbb{C}[\mathfrak{S}_n])$ is an algebra contained in $\text{End}_{SU(2)}(W)$, any polynomial in $\{\Pi(\sigma)\}$ (hence the exponential) is $SU(2)$ -equivariant. Additionally, if $\sum_j c_j \Pi(\sigma_j)$ is anti-Hermitian, then Q is unitary and usable as a quantum gate.

Generalized Permutation to $SU(2)$ Equivariant Gate. Let $W := V^{\otimes n}$. We show that every invertible $SU(2)$ -equivariant operator (in particular, every unitary gate) T on W is a generalized permutation: $T = \exp[\sum_{j=1}^m c_j \Pi(\sigma_j)]$.

Proof. By the Schur–Weyl duality (double-commutant form),

$$\text{End}_{SU(2)}(W) = \Pi(\mathbb{C}[\mathfrak{S}_n]) =: \mathcal{A}, \quad (72)$$

a finite-dimensional $*$ -algebra (i.e., a finite-dimensional algebra equipped with an adjoint operation (conjugate-linear, reverses multiplication, and applying it twice returns the original element)). If T is $SU(2)$ -equivariant, then $T \in \mathcal{A}$. Since T is invertible (unitary suffices), the holomorphic functional calculus in the finite-dimensional algebra \mathcal{A} provides a logarithm $\log T \in \mathcal{A}$ such that $\exp(\log T) = T$. Because \mathcal{A} is the linear span of $\{\Pi(\sigma) : \sigma \in \mathfrak{S}_n\}$, there exist $c_1, \dots, c_m \in \mathbb{C}$ and $\sigma_1, \dots, \sigma_m \in \mathfrak{S}_n$ with

$$\log T = \sum_{j=1}^m c_j \Pi(\sigma_j). \quad (73)$$

Exponentiating gives

$$T = \exp\left(\sum_{j=1}^m c_j \Pi(\sigma_j)\right), \quad (74)$$

so T is a generalized permutation.

A.7. Group Twirling.

We show that $\mathcal{T}_G[A]$ commutes with the group action, i.e., it is G -equivariant as an operator. For any fixed $\tau \in G$,

$$\begin{aligned} V[\tau] \mathcal{T}_G[A] &= \frac{1}{|G|} \sum_{g \in G} V[\tau] V[g] A V[g]^{-1} = \frac{1}{|G|} \sum_{g \in G} V[\tau g] A V[g]^{-1} \\ &\stackrel{g'=\tau g}{=} \frac{1}{|G|} \sum_{g' \in G} V[g'] A V[\tau^{-1} g']^{-1} = \frac{1}{|G|} \sum_{g' \in G} V[g'] A V[g']^{-1} V[\tau] \\ &= \mathcal{T}_G[A] V[\tau], \end{aligned} \quad (75)$$

where we used $(\tau^{-1}g')^{-1} = g'^{-1}\tau$ and the homomorphism property of V . Hence $\mathcal{T}_G[A]$ lies in the commutant

$$\{M \in \text{End}(W) : M V[\tau] = V[\tau] M, \forall \tau \in G\}, \quad (76)$$

and is therefore invariant under the adjoint (conjugation) action of G . For a unitary representation, we can write $V[\tau]^{-1}$ as $V[\tau]^\dagger$.

B. Quantum Network

B.1. Singlet State

Singlet State Definition The two qubit singlet

$$|\psi^-\rangle := \frac{|01\rangle - |10\rangle}{\sqrt{2}} \quad (77)$$

is the unique spin-0 ($j = 0$) irreducible component inside

$$\frac{1}{2} \otimes \frac{1}{2} = 0 \oplus 1. \quad (78)$$

Equivalently, it spans the one-dimensional $j = 0$ irrep.

SU(2)-invariance. Let $\rho(U) = U^{\otimes 2}$ denote the diagonal action of $U \in \text{SU}(2)$ on two qubits. Then

$$\rho(U)|\psi^-\rangle = |\psi^-\rangle \quad (\forall U \in \text{SU}(2)). \quad (79)$$

Proof. Let $T = \text{SWAP}$ on $\mathbb{C}^2 \otimes \mathbb{C}^2$. Since T is an involution ($T^2 = I$) with eigenvalues ± 1 , we have the eigenspace decomposition

$$\mathbb{C}^2 \otimes \mathbb{C}^2 = \text{Sym}^2(\mathbb{C}^2) \oplus \wedge^2(\mathbb{C}^2), \quad \dim \text{Sym}^2(\mathbb{C}^2) = 3, \dim \wedge^2(\mathbb{C}^2) = 1, \quad (80)$$

where $E_{+1}(T) = \text{Sym}^2(\mathbb{C}^2)$ and $E_{-1}(T) = \wedge^2(\mathbb{C}^2)$

The vector $|\psi^-\rangle$ is antisymmetric under the qubit swap (i.e., $\text{SWAP}|\psi^-\rangle = -|\psi^-\rangle$), so $|\psi^-\rangle \in \wedge^2(\mathbb{C}^2)$; since $\dim \wedge^2(\mathbb{C}^2) = 1$, it follows that

$$\wedge^2(\mathbb{C}^2) = \text{span}\{|\psi^-\rangle\}. \quad (81)$$

Now consider $U \in \text{SU}(2)$ and the diagonal action $\rho(U) = U^{\otimes 2}$. Since SWAP permutes tensor factors, it commutes with $U \otimes U$, and hence $\wedge^2(\mathbb{C}^2)$ is $\rho(U)$ -invariant, up to a phase factor. We can further show that the phase factor must be 1 from the following argument. Since $\dim \wedge^2(\mathbb{C}^2) = 1$, there exists a phase $\chi(U) \in \text{U}(1)$ such that $(U \otimes U)|\psi^-\rangle = \chi(U)|\psi^-\rangle$. But the induced action on $\wedge^2(\mathbb{C}^2)$ is $\wedge^2 U = \det(U) I$, so $\chi(U) = \det(U) = 1$ for $U \in \text{SU}(2)$; hence $(U \otimes U)|\psi^-\rangle = |\psi^-\rangle$.

B.2. Geometric Encoding

From $\text{SU}(2)$ to 3D rotations. As shown in Appendix A.2, unitary conjugation by $U_R \in \text{SU}(2)$ induces a 3D rotation on Pauli vectors:

$$U_R(\vec{v} \cdot \vec{\sigma})U_R^\dagger = \sum_{i,j} R_{ij}(U_R)v_j \sigma_i = (R(U_R)\vec{v}) \cdot \vec{\sigma}, \quad (82)$$

where $\Phi : U \mapsto R(U)$ is a group homomorphism $\text{SU}(2) \rightarrow \text{SO}(3)$. This lets us convert rotations of 3D points into unitary transformations of qubits.

Geometric Encoding's Rotation Equivariance. Let $\Phi : \text{SU}(2) \rightarrow \text{SO}(3)$ be the covering homomorphism. For any $R \in \text{SO}(3)$ pick $U_R \in \text{SU}(2)$ with $\Phi(U_R) = R$. Since $\|\mathbf{p}\|$ is rotation-invariant and $R\mathbf{p} = \mathbf{p}'$, we have

$$E(\mathbf{p}') = \exp\left(i \frac{\|\mathbf{p}\|}{\Theta} (R\hat{\mathbf{p}}) \cdot \vec{\sigma}\right) \quad (83)$$

$$= \exp\left(i \frac{\|\mathbf{p}\|}{\Theta} U_R(\hat{\mathbf{p}} \cdot \vec{\sigma})U_R^\dagger\right) \quad (\text{by (82)}) \quad (84)$$

$$= U_R \exp\left(i \frac{\|\mathbf{p}\|}{\Theta} \hat{\mathbf{p}} \cdot \vec{\sigma}\right) U_R^\dagger \quad (85)$$

$$= U_R E(\mathbf{p}) U_R^\dagger. \quad (86)$$

Hence the encoder is exactly rotation equivariant (via $SU(2)$ adjoint action):

$$E(R\mathbf{p}) = U_R E(\mathbf{p}) U_R^\dagger, \quad \Phi(U_R) = R. \quad (87)$$

Quantum Gate Expression. For practical quantum circuit implementation, encodings must be decomposed into elementary single qubit gates supported by current hardware. We encode each 3D point $\mathbf{p}_i \in \mathbb{R}^3$ by the unitary

$$E(\mathbf{p}_i) = \exp\left(i \frac{\|\mathbf{p}_i\|}{\Theta} \hat{\mathbf{p}}_i \cdot \vec{\sigma}\right) = R_Z(\alpha_i) R_Y(\beta_i) R_Z(\gamma_i), \quad (88)$$

i.e., we exactly realize the exponential as a Z–Y–Z sequence on each encoding qubit i . Here $\Theta > 0$ is a fixed geometric scale, $\hat{\mathbf{p}}_i = \mathbf{p}_i / \|\mathbf{p}_i\|$ and $\vec{\sigma} = (\sigma_x, \sigma_y, \sigma_z)$.

Given the preprocessed point cloud, we first normalize by Θ :

$$\tilde{\mathbf{p}}_i = \mathbf{p}_i / \Theta, \quad \phi_i = \|\tilde{\mathbf{p}}_i\|, \quad \mathbf{n}_i = \tilde{\mathbf{p}}_i / \|\tilde{\mathbf{p}}_i\| = (n_x, n_y, n_z). \quad (89)$$

The Z–Y–Z angles are

$$\alpha_i = \arctan(-n_z \tan \phi_i) + \arctan\left(\frac{-n_x}{n_y}\right), \quad (90)$$

$$\gamma_i = \arctan(-n_z \tan \phi_i) - \arctan\left(\frac{-n_x}{n_y}\right), \quad (91)$$

$$\beta_i = 2 \arcsin\left(\frac{\sin \phi_i n_x}{\sin((\alpha_i - \gamma_i)/2)}\right). \quad (92)$$

In practice, we use `arctan2` for robust angle-branch (quadrant) selection, which remains well-defined even when $n_y = 0$. Axis-aligned degenerate cases (e.g., $n_x = n_y = 0$) are handled separately.

On the Scale Θ . The angle formulas involve $\tan(\phi_i)$ and an $\arcsin(\cdot)$ in β_i , both of which are numerically sensitive: $\tan(\cdot)$ becomes ill-conditioned near $(k + \frac{1}{2})\pi$, and $\arcsin(\cdot)$ requires inputs in $[-1, 1]$ with margins to avoid floating-point clipping. To improve stability, we set the geometric scale Θ larger than the maximum point cloud radius, so that $\phi_i = \|\mathbf{p}_i\|/\Theta$ stays well within numerically benign regions and the \arcsin argument remains bounded away from ± 1 . We then performed hyperparameter tuning over several Θ values under this constraint and found that a single fixed $\Theta = 1.7$ works well for most instances, which we also used for all reported experiments.

Pair Selective Encoding and Permutation. To obtain a pairwise permutation-equivariant quantum part while preserving the singlet structure, we encode one qubit per pair $(2j, 2j+1)$:

$$|\Psi_{\text{enc}}\rangle = \bigotimes_{j=0}^{N-1} (E(\mathbf{p}_j) \otimes I) |\psi^-\rangle_{(2j, 2j+1)}, \quad |\psi^-\rangle = \frac{1}{\sqrt{2}}(|01\rangle - |10\rangle). \quad (93)$$

Here $E(\mathbf{p})$ is the single-qubit encoding unitary.

We used per-pair encoding to make the effect of permutation consistent for any $\sigma \in \mathfrak{S}_N$. If two distinct points are fed to one pair,

$$|\Psi(\mathbf{p}_a, \mathbf{p}_b)\rangle = (E(\mathbf{p}_a) \otimes E(\mathbf{p}_b)) |\psi^-\rangle, \quad (94)$$

then swapping the two inputs gives

$$S |\Psi(\mathbf{p}_a, \mathbf{p}_b)\rangle = (E(\mathbf{p}_b) \otimes E(\mathbf{p}_a)) S |\psi^-\rangle = - (E(\mathbf{p}_b) \otimes E(\mathbf{p}_a)) |\psi^-\rangle = - |\Psi(\mathbf{p}_b, \mathbf{p}_a)\rangle, \quad (95)$$

which implies that the within-pair wire swap changes only the global phase, and since the global phase does not affect any physical outcomes, this effect cannot be observed. In contrast, consider four qubits initialized as two singlet pairs, $|\psi^-\rangle_{01} \otimes |\psi^-\rangle_{23}$, and let $\Pi_{(0,3)}$ denote the SWAP between wires 0 and 3. Define $E_i := E(\mathbf{p}_i)$ and

$$|\Psi(\mathbf{p}_0, \mathbf{p}_1, \mathbf{p}_2, \mathbf{p}_3)\rangle := (E_0 \otimes E_1) |\psi^-\rangle_{01} \otimes (E_2 \otimes E_3) |\psi^-\rangle_{23}. \quad (96)$$

For the point-permutation $\sigma = (0\ 3)$ (acting on inputs only),

$$|\Psi(\mathbf{p}_3, \mathbf{p}_1, \mathbf{p}_2, \mathbf{p}_0)\rangle = (E_3 \otimes E_1)|\psi^-\rangle_{01} \otimes (E_2 \otimes E_0)|\psi^-\rangle_{23}. \quad (97)$$

This state is product across $(01) \mid (23)$, hence the reduced state on wires $(0, 1)$ is pure:

$$\rho_{01}^{(\sigma)} := \text{Tr}_{23} \left[|\Psi(\mathbf{p}_3, \mathbf{p}_1, \mathbf{p}_2, \mathbf{p}_0)\rangle \langle \Psi(\mathbf{p}_3, \mathbf{p}_1, \mathbf{p}_2, \mathbf{p}_0)| \right], \quad \text{rank}(\rho_{01}^{(\sigma)}) = 1. \quad (98)$$

Now let $\Pi_{(0,3)}$ swap wires 0 and 3. Then

$$\Pi_{(0,3)}|\Psi(\mathbf{p}_0, \mathbf{p}_1, \mathbf{p}_2, \mathbf{p}_3)\rangle = (E_3 \otimes E_1 \otimes E_2 \otimes E_0) (|\psi^-\rangle_{31} \otimes |\psi^-\rangle_{20}). \quad (99)$$

Taking the reduced state on wires $(0, 1)$ and using $\text{Tr}_q |\psi^-\rangle \langle \psi^-| = \frac{I}{2}$ gives

$$\rho_{01}^{(\Pi_{(0,3)})} := \text{Tr}_{23} \left[\Pi_{(0,3)}|\Psi(\mathbf{p}_0, \mathbf{p}_1, \mathbf{p}_2, \mathbf{p}_3)\rangle \langle \Psi(\mathbf{p}_0, \mathbf{p}_1, \mathbf{p}_2, \mathbf{p}_3)| \Pi_{(0,3)}^\dagger \right] = \frac{I_{01}}{4}, \quad \text{rank}(\rho_{01}^{(\Pi_{(0,3)})}) = 4, \quad (100)$$

Therefore, the two states cannot be proportional (even up to a global phase):

$$\Pi_{(0,3)}|\Psi(\mathbf{p}_0, \mathbf{p}_1, \mathbf{p}_2, \mathbf{p}_3)\rangle \not\propto |\Psi(\mathbf{p}_3, \mathbf{p}_1, \mathbf{p}_2, \mathbf{p}_0)\rangle, \quad (101)$$

Thus, a two points per pair encoding is not necessarily permutation equivariant. The pair selective scheme (93) is the effective compromise used in our experiments: with n qubits arranged into $n/2$ singlet pairs, one can encode $n/2$ points while maintaining permutation equivariance.

Nonexistence of nontrivial joint rotation–permutation invariants. Fix $n \geq 1$ and consider the n -qubit Hilbert space $\mathcal{H} := (\mathbb{C}^2)^{\otimes n}$. We let $\text{SU}(2)$ act by global spin rotations $U^{\otimes n}$ and \mathfrak{S}_n act by permuting tensor factors via permutation operators P_σ . Then the joint fixed-point subspace is trivial:

$$\mathcal{H}^{\text{SU}(2)} \cap \mathcal{H}^{\mathfrak{S}_n} = \{0\}. \quad (102)$$

Proof. The actions of $\text{SU}(2)$ and \mathfrak{S}_n commute, hence \mathcal{H} carries a representation of $\text{SU}(2) \times \mathfrak{S}_n$. A state $|\psi\rangle \in \mathcal{H}$ is invariant under both rotations and permutations if and only if

$$U^{\otimes n}|\psi\rangle = |\psi\rangle \quad \forall U \in \text{SU}(2), \quad \Pi(\sigma)|\psi\rangle = |\psi\rangle \quad \forall \sigma \in \mathfrak{S}_n. \quad (103)$$

Equivalently, $|\psi\rangle$ must lie in the tensor product of the trivial irrep of $\text{SU}(2)$ and the trivial irrep of \mathfrak{S}_n inside the Schur–Weyl decomposition of \mathcal{H} .

By Schur–Weyl duality, we have the decomposition

$$\mathcal{H} \cong \bigoplus_{\lambda \vdash n, \ell(\lambda) \leq 2} V_\lambda^{\text{SU}(2)} \otimes V_\lambda^{\mathfrak{S}_n}, \quad (104)$$

where the sum ranges over partitions λ of n with at most two rows. For n qubits (spin- $\frac{1}{2}$ systems), the admissible total spins are $J = \frac{n}{2}, \frac{n}{2} - 1, \dots$, and the partition corresponding to spin J is

$$\lambda(J) = \left(\frac{n}{2} + J, \frac{n}{2} - J \right), \quad (105)$$

so that the fully symmetric subspace (partition (n)) corresponds to the highest spin $J = \frac{n}{2}$, while the singlet (spin-0) subspace (for even n) corresponds to the partition $(\frac{n}{2}, \frac{n}{2})$. In particular, all $\text{SU}(2)$ -invariant vectors lie in the singlet block

$$V_{\lambda(0)}^{\text{SU}(2)} \otimes V_{\lambda(0)}^{\mathfrak{S}_n}, \quad \lambda(0) = \left(\frac{n}{2}, \frac{n}{2} \right), \quad (106)$$

which exists only when n is even. On the other hand, the trivial irrep of \mathfrak{S}_n appears exactly once and corresponds to the fully symmetric partition $\lambda_{\text{sym}} = (n)$, i.e., it sits in the summand

$$V_{\lambda_{\text{sym}}}^{\text{SU}(2)} \otimes V_{\lambda_{\text{sym}}}^{\mathfrak{S}_n} \quad \text{with} \quad \lambda_{\text{sym}} = (n), \quad J(\lambda_{\text{sym}}) = \frac{n}{2}. \quad (107)$$

Thus, $\text{SU}(2)$ -invariant vectors live in the $\lambda(0)$ block, whereas \mathfrak{S}_n -invariant vectors live in the λ_{sym} block, and these blocks are distinct:

$$\lambda(0) = \left(\frac{n}{2}, \frac{n}{2} \right) \neq (n) = \lambda_{\text{sym}} \quad \text{for all even } n \geq 2. \quad (108)$$

In particular, there is no summand of the form (trivial $\text{SU}(2)$ irrep) \otimes (trivial \mathfrak{S}_n irrep) inside the Schur–Weyl decomposition of $(\mathbb{C}^2)^{\otimes n}$ for any $n \geq 1$. It follows that the only vector invariant under both global rotations $U^{\otimes n}$ and all permutations P_σ is the zero vector. In other words, there is no nontrivial state that is simultaneously invariant under $\text{SU}(2)$ and \mathfrak{S}_n .

B.3. Our Quantum Network via Twirling

Derivation of the pair-symmetrized blocks P_k^\pm . We recall the notations from Section 4.3. The $n = 2N$ wires are grouped into disjoint pairs

$$B_\ell := \{2\ell, 2\ell + 1\}, \quad \ell = 0, \dots, N - 1, \quad (109)$$

and we define the pair-permuting subgroup

$$\mathfrak{S}_{\text{pair}} := \{\sigma : \{B_\ell\} \rightarrow \{B_\ell\} \mid \sigma \text{ is bijective}\} \leq \mathfrak{S}_{2N}, \quad (110)$$

which acts by permuting these pairs as whole blocks while leaving the internal structure of each pair intact.

We denote Π by the permutation representation of \mathfrak{S}_n on the n wires. For any finite subgroup $H \subseteq \mathfrak{S}_n$, we define the (operator) twirl on $M \in \mathbb{C}^{2^n \times 2^n}$ by

$$\mathcal{T}_H[M] := \frac{1}{|H|} \sum_{h \in H} \Pi(h) M \Pi(h)^\dagger. \quad (111)$$

In particular, in our quantum circuit architecture, we use $H = \mathfrak{S}_{\text{pair}}$.

Fix $2 \leq k \leq N$ and consider all ordered selections of k distinct pairs from the N available pairs. Let

$$\mathcal{P} = \{(0, 1), (2, 3), \dots, (n - 2, n - 1)\} \quad (112)$$

be the set of pairs, and write $\text{Perm}(\mathcal{P}, k)$ for the set of ordered k -tuples. For a given $\pi = (p_1, \dots, p_k) \in \text{Perm}(\mathcal{P}, k)$ where $p_m = (2j_m, 2j_m + 1)$ and a selection vector $\mathbf{s} = (s_1, \dots, s_k) \in \{0, 1\}^k$, we define $\tau_\pi^\mathbf{s} \in GL(\mathcal{H}) \subset \mathbb{C}^{2^n \times 2^n}$ to be the permutation matrix representing the k -cycle

$$(2j_1 + s_1, 2j_2 + s_2, \dots, 2j_k + s_k). \quad (113)$$

on the selected wires and leaves all other wires fixed. Intuitively, for each pair B_{i_ℓ} we choose either its first wire ($s_\ell = 0$) or second wire ($s_\ell = 1$) to participate in the cycle, while the partner wire in the same pair stays put.

For a fixed interaction order k and an ordered k -tuple of pairs $\pi \in \text{Perm}(\mathcal{P}, k)$, we defined a class of generalized k -cycle generators supported on these pairs by

$$M_{k, \pi}^{(w)} := \sum_{\mathbf{s} \in \{0, 1\}^k} w(\mathbf{s}) \tau_\pi^\mathbf{s}, \quad (114)$$

where $w : \{0, 1\}^k \rightarrow \mathbb{C}$ determines the coefficient for 2^k choices of within-pair selections. Our goal is to endow these already rotation-equivariant operators with $\mathfrak{S}_{\text{pair}}$ -equivariance, which can be achieved in principle by twirling any generalized permutation under $\mathfrak{S}_{\text{pair}}$.

While the twirling can be applied to any arbitrary operators, we restrict the operators to those with the coefficients defined as

$$w^{(+)}(\mathbf{s}) := 1, \quad w^{(-)}(\mathbf{s}) := (-1)^{\|\mathbf{s}\|_1}, \quad (115)$$

which are natural choice from the structure of $\mathfrak{S}_{\text{pair}}$, where $\|\mathbf{s}\|_1$ is the Hamming weight of \mathbf{s} . The corresponding operators are given as

$$M_{k, \pi}^{(+)} := \sum_{\mathbf{s} \in \{0, 1\}^k} \tau_\pi^\mathbf{s}, \quad M_{k, \pi}^{(-)} := \sum_{\mathbf{s} \in \{0, 1\}^k} (-1)^{\|\mathbf{s}\|_1} \tau_\pi^\mathbf{s}. \quad (116)$$

We now compute the pair-permuting twirl of these two special combinations and show that they give precisely P_k^+ and P_k^- .

Uniform pattern. Using the definition of the pair-permuting twirl and the conjugation rule $\Pi(\sigma) \tau_\pi^\mathbf{s} \Pi(\sigma)^\dagger = \tau_{\sigma\pi}^\mathbf{s}$ for $\sigma \in \mathfrak{S}_{\text{pair}}$, we get

$$\begin{aligned} \mathcal{T}_{\mathfrak{S}_{\text{pair}}}[M_{k, \pi}^{(+)}] &= \frac{1}{|\mathfrak{S}_{\text{pair}}|} \sum_{\sigma \in \mathfrak{S}_{\text{pair}}} \Pi(\sigma) \left(\sum_{\mathbf{s}} \tau_\pi^\mathbf{s} \right) \Pi(\sigma)^\dagger \\ &= \frac{1}{|\mathfrak{S}_{\text{pair}}|} \sum_{\sigma \in \mathfrak{S}_{\text{pair}}} \sum_{\mathbf{s}} \tau_{\sigma\pi}^\mathbf{s}. \end{aligned} \quad (117)$$

The induced action of $S_{\text{pair}} \cong S_N$ on ordered k -tuples of distinct pairs is transitive: for any $\pi, \pi' \in \text{Perm}(\mathcal{P}, k)$ there exists $\sigma \in \mathfrak{S}_{\text{pair}}$ such that $\sigma \cdot \pi = \pi'$. For a fixed π , let us

$$\text{Stab}(\pi) := \{\sigma \in \mathfrak{S}_{\text{pair}} : \sigma \cdot \pi = \pi\} \quad (118)$$

denote by its stabilizer. In our setting, keeping the ordered list of k active pairs $(B_{i_1}, \dots, B_{i_k})$ fixed forces σ to permute only the remaining $N - k$ inactive pairs, so $|\text{Stab}(\pi)| = (N - k)!$ depends only on N and k , but not on the particular choice of π . By the orbit-stabilizer theorem,

$$|\mathfrak{S}_{\text{pair}}| = |\text{Orbit}(\pi)| \cdot |\text{Stab}(\pi)| = |\text{Perm}(\mathcal{P}, k)| \cdot |\text{Stab}(\pi)|, \quad (119)$$

and for every $\pi' \in \text{Perm}(\mathcal{P}, k)$ the number of $\sigma \in \mathfrak{S}_{\text{pair}}$ with $\sigma \cdot \pi = \pi'$ is exactly $|\text{Stab}(\pi)|$. Thus each π' appears equally often in the multiset $\{\sigma \cdot \pi : \sigma \in \mathfrak{S}_{\text{pair}}\}$, and the average over σ is proportional to the uniform average over all ordered k -tuples:

$$\frac{1}{|\mathfrak{S}_{\text{pair}}|} \sum_{\sigma \in \mathfrak{S}_{\text{pair}}} \sum_{\mathbf{s} \in \{0,1\}^k} \tau_{\sigma\pi}^{\mathbf{s}} \propto \frac{1}{k!} \sum_{\pi' \in \text{Perm}(\mathcal{P}, k)} \sum_{\mathbf{s} \in \{0,1\}^k} \tau_{\pi'}^{\mathbf{s}}. \quad (120)$$

In particular, for the uniform pattern $M_{k,\pi}^{(+)} := \sum_{\mathbf{s} \in \{0,1\}^k} \tau_{\pi}^{\mathbf{s}}$, we obtain

$$\mathcal{T}_{\mathfrak{S}_{\text{pair}}} [M_{k,\pi}^{(+)}] \propto \frac{1}{k!} \sum_{\pi' \in \text{Perm}(\mathcal{P}, k)} \sum_{\mathbf{s} \in \{0,1\}^k} \tau_{\pi'}^{\mathbf{s}} = P_k^+. \quad (121)$$

Parity pattern. The computation for the parity-weighted pattern is identical, except that the factor $(-1)^{\|\mathbf{s}\|_1}$ does not depend on the pair indices and is therefore unchanged by the $\mathfrak{S}_{\text{pair}}$ action:

$$\begin{aligned} \mathcal{T}_{\mathfrak{S}_{\text{pair}}} [M_{k,\pi}^{(-)}] &= \frac{1}{|\mathfrak{S}_{\text{pair}}|} \sum_{\sigma \in \mathfrak{S}_{\text{pair}}} \Pi(\sigma) \left(\sum_{\mathbf{s}} (-1)^{\|\mathbf{s}\|_1} \tau_{\pi}^{\mathbf{s}} \right) \Pi(\sigma)^\dagger \\ &= \frac{1}{|\mathfrak{S}_{\text{pair}}|} \sum_{\sigma \in \mathfrak{S}_{\text{pair}}} \sum_{\mathbf{s}} (-1)^{\|\mathbf{s}\|_1} \tau_{\sigma\pi}^{\mathbf{s}} \\ &\propto \frac{1}{k!} \sum_{\pi' \in \text{Perm}(\mathcal{P}, k)} \sum_{\mathbf{s} \in \{0,1\}^k} (-1)^{\|\mathbf{s}\|_1} \tau_{\pi'}^{\mathbf{s}} = P_k^-. \end{aligned} \quad (122)$$

Unitarity of the Quantum Network. On a quantum device, every implemented gate must be unitary. In particular, each phase factor of the form $e^{ic_k^\pm P_k^\pm}$ used in our network must be unitary. We verify this by showing that the operators P_k^\pm are Hermitian, and then invoking a standard fact about exponentials of Hermitian operators.

The definition in the main text, P_k^+ and P_k^- are (up to normalization) finite linear combinations of the permutation matrices $\tau_{\pi'}^{\mathbf{t}}$:

$$P_k^+ \propto \sum_{\pi' \in \text{Perm}(\mathcal{P}, k)} \sum_{\mathbf{t} \in \{0,1\}^k} \tau_{\pi'}^{\mathbf{t}}, \quad P_k^- \propto \sum_{\pi' \in \text{Perm}(\mathcal{P}, k)} \sum_{\mathbf{t} \in \{0,1\}^k} (-1)^{\|\mathbf{t}\|_1} \tau_{\pi'}^{\mathbf{t}}. \quad (123)$$

Each $\tau_{\pi'}^{\mathbf{t}}$ is a permutation matrix and hence unitary, so

$$(\tau_{\pi'}^{\mathbf{t}})^\dagger = (\tau_{\pi'}^{\mathbf{t}})^{-1}. \quad (124)$$

The inverse of the k -cycle implemented by $\tau_{\pi'}^{\mathbf{t}}$ is the same cycle with the order of its k support wires reversed, which is again of the form $\tau_{\pi''}^{\mathbf{t}'}$ for some ordered k -tuple π'' . Since we sum over all ordered k -tuples of distinct pairs, the index set $\{(\pi', \mathbf{t})\}$ is closed under inversion: for every (π', \mathbf{t}) there is (π'', \mathbf{t}') with

$$(\tau_{\pi'}^{\mathbf{t}})^{-1} = \tau_{\pi''}^{\mathbf{t}'}. \quad (125)$$

Using this closure under inversion, we obtain

$$(P_k^+)^* \propto \sum_{\pi', \mathbf{t}} (\tau_{\pi'}^{\mathbf{t}})^* = \sum_{\pi', \mathbf{t}} (\tau_{\pi'}^{\mathbf{t}})^{-1} = \sum_{\pi'', \mathbf{t}'} \tau_{\pi''}^{\mathbf{t}'} \propto P_k^+, \quad (126)$$

where the last step is just a relabeling of the summation index $(\pi', \mathbf{t}) \mapsto (\pi'', \mathbf{t}')$. Similarly,

$$(P_k^-)^\dagger \propto \sum_{\pi', \mathbf{t}} (-1)^{\|\mathbf{t}\|_1} (\tau_{\pi'}^{\mathbf{t}})^\dagger = \sum_{\pi', \mathbf{t}} (-1)^{\|\mathbf{t}\|_1} (\tau_{\pi'}^{\mathbf{t}})^{-1} = \sum_{\pi'', \mathbf{t}'} (-1)^{\|\mathbf{t}'\|_1} (\tau_{\pi''}^{\mathbf{t}'}) \propto P_k^-, \quad (127)$$

since inversion may permute the coordinates of the selection vector \mathbf{t} (i.e., $\mathbf{t}' = \rho \cdot \mathbf{t}$ for some $\rho \in \mathfrak{S}_k$), but it preserves the Hamming weight $\|\mathbf{t}\|_1$, hence $(-1)^{\|\mathbf{t}'\|_1} = (-1)^{\|\mathbf{t}\|_1}$. After fixing normalizations, this shows that

$$(P_k^\pm)^\dagger = P_k^\pm, \quad (128)$$

i.e., both P_k^+ and P_k^- are Hermitian.

To conclude that

$$U_k^\pm := e^{ic_k^\pm P_k^\pm} \quad (129)$$

is unitary for every real coefficient $c_k^\pm \in \mathbb{R}$, it suffices to recall a standard fact: whenever H is Hermitian and $c \in \mathbb{R}$, the exponential

$$U := e^{icH} \quad (130)$$

is unitary.

B.4. Heisenberg Hamiltonian

Hamiltonian and expectation value. A Hamiltonian H is a Hermitian operator acting on the system Hilbert space \mathcal{H} . Its physical prediction is the energy expectation $\langle H \rangle_\rho := \text{Tr}(\rho H)$ for a density operator ρ , which reduces to $\langle \psi | H | \psi \rangle$ for a pure state $|\psi\rangle$. We consider N spin- $\frac{1}{2}$ degrees of freedom arranged on a graph $G = (V, E)$ where edges indicate pairs that interact. At site $i \in V$, let $\vec{S}_i = (S_i^x, S_i^y, S_i^z)$ denote the spin operators with the standard normalization $S_i^\alpha = \frac{\hbar}{2} \sigma_i^\alpha$, where σ_i^α are Pauli matrices acting nontrivially only on site i .

Heisenberg Hamiltonian. Let $G = (V, E)$ be an undirected interaction graph. The (isotropic) Heisenberg Hamiltonian is

$$H = J \sum_{\langle i, j \rangle \in E} \vec{S}_i \cdot \vec{S}_j = J \sum_{\langle i, j \rangle \in E} \sum_{\alpha \in \{x, y, z\}} S_i^\alpha S_j^\alpha = \frac{J \hbar^2}{4} \sum_{\langle i, j \rangle \in E} \sum_{\alpha \in \{x, y, z\}} \sigma_i^\alpha \sigma_j^\alpha, \quad (131)$$

where $J \in \mathbb{R}$ is the exchange coupling (ferromagnetic $J < 0$, antiferromagnetic $J > 0$), and $S_i^\alpha = \frac{\hbar}{2} \sigma_i^\alpha$.

SU(2) invariance. Let $U \in \text{SU}(2)$ act globally as $U^{\otimes N}$. The adjoint action rotates spin components: there exists $R(U) \in \text{SO}(3)$ such that

$$U S_i^\alpha U^\dagger = \sum_{\beta \in \{x, y, z\}} R_{\alpha\beta}(U) S_i^\beta, \quad \text{or equivalently,} \quad U (\vec{S}_i \cdot \vec{v}) U^\dagger = \vec{S}_i \cdot (R(U) \vec{v}). \quad (132)$$

Hence, each pairwise scalar product is invariant:

$$U^{\otimes 2} (\vec{S}_i \cdot \vec{S}_j) (U^\dagger)^{\otimes 2} = \sum_{\alpha} (U^{\otimes 2} S_i^\alpha (U^\dagger)^{\otimes 2}) (U^{\otimes 2} S_j^\alpha (U^\dagger)^{\otimes 2}) = \sum_{\alpha, \beta, \gamma} R_{\alpha\beta}(U) R_{\alpha\gamma}(U) S_i^\beta S_j^\gamma \quad (133)$$

$$= \sum_{\beta, \gamma} (R(U)^\top R(U))_{\beta\gamma} S_i^\beta S_j^\gamma = \sum_{\beta} S_i^\beta S_j^\beta = \vec{S}_i \cdot \vec{S}_j, \quad (134)$$

using orthogonality $R(U)^\top R(U) = I$. Summing over $(i, j) \in E$ yields

$$U^{\otimes N} H (U^{\otimes N})^\dagger = H, \quad (135)$$

i.e., the Heisenberg Hamiltonian is globally SU(2)-invariant.

Table 2. Compute environments by run group.

Group	Datasets	Hardware
Classical Baselines	All datasets	Apple M4 chip
RP-EQGN	All datasets	NVIDIA A100
HyQuRP ($N=4$)	All datasets	Apple M4 chip
HyQuRP ($N=5$)	All datasets	NVIDIA A100
HyQuRP ($N=6$)	All datasets	NVIDIA H100

C. Additional Experimental Details

C.1. Data Construction

We evaluate on three object-level datasets using small-class subsets: ModelNet-5 (bottle, bowl, cup, lamp, stool), ShapeNet-5 (birdhouse, bottle, bowl, bus, cap), and Sydney Urban Objects-3 (car, traffic sign, pedestrian). The original taxonomies contain ModelNet40 (40 classes), ShapeNetCore (55 classes), and Sydney Urban Objects (14 classes). To increase the reliability of our comparisons under sparse-point budgets, we select five classes for the relatively clean CAD datasets (ModelNet/ShapeNet) and three for the more challenging real-world LiDAR dataset (Sydney Urban Objects).

For each normalized object, we first form a dense candidate set of surface points (typically $\sim 2,048$ candidates). Candidates are drawn from the underlying geometry representation (mesh surface for CAD, LiDAR returns for SUO) to cover the shape broadly. Objects are partitioned into training, validation, and test sets. For ModelNet, we follow the official train/test split and reserve a portion of the training data for validation; for all other datasets, splits are constructed using disjoint sets of objects. Given a point budget of N , we maintain class-balanced splits with a 7:1:2 ratio, resulting in $700N$, $100N$, and $200N$ points per class for training, validation, and testing, respectively. For $N \in \{4, 5, 6\}$, points are selected via farthest point sampling (FPS) with a random initial seed. This iterative process selects the candidate furthest from the current set to maximize spatial coverage and minimize redundancy. To ensure sample diversity, points are sampled without replacement. For the Sydney Urban Objects dataset—where the candidate pool may be smaller than N —we supplement the selection via random sampling from the residual pool, employing replacement only when necessary while minimizing index collisions. ModelNet and ShapeNet require no such supplementation.

We summarize data preprocessing for each dataset as follows:

- ModelNet-5: We use the widely adopted HDF5 release (modelnet40_ply_hdf5_2048), which provides 2,048 pre-sampled surface points per object derived from the official meshes. We run the FPS on the provided candidate set to select N points. We do not apply any additional centering or unit max-radius scaling, since the released data are already centered and unit max-radius scaled. Additionally, compared to ShapeNet, intra-class variation is smaller, and the models are cleaner.
- ShapeNet-5: We draw a dense candidate set by area-weighted uniform sampling over the mesh surface. We then center and unit max-radius scale the candidates and apply FPS to obtain N points.
- Sydney Urban Objects-3: Candidates are taken from object-level LiDAR returns after centering and unit max-radius scaling; occlusions and sensor noise make the distribution sparse and anisotropic, hence FPS is particularly helpful to avoid clustered selections.

C.2. Implementation Settings

Hardware mappings are listed in Tab. 2. Classical baselines can be run on local hardware, whereas quantum baselines typically require substantially more memory due to the exponential growth of the Hilbert space with the number of qubits. For example, HyQuRP caches $2(N - 1)$ unitary matrices of size $2^{2N} \times 2^{2N}$ (from the eigendecompositions of the twirling operators), which makes large-memory GPUs (e.g., A100 or H100) necessary in our experiments.

We use Adam, batch size of 35, and train for 1000 epochs. For each model, the same learning rate η is used for all datasets and $N \in \{4, 5, 6\}$, which is optimized for the ModelNet dataset with $N = 4$ over $\eta \in \{10^{-2}, 10^{-3}, 10^{-4}\}$. We do not use schedulers, weight decay, dropout, or early stopping. Model selection uses the validation accuracy: we report the best top-1

Table 3. Training protocol.

Setting	Value
Augmentation	random point permutation, rotation and jitter
Optimizer	Adam
Loss function	cross-entropy
Batch size	35
Epochs	1000
Learning rate	optimized for the ModelNet with $N=4$ from $\{10^{-2}, 10^{-3}, 10^{-4}\}$ is used for all other dataset
Selection rule	best validation accuracy epoch
Seeds	7 (121, 831, 1557, 2023–2026)
Regularization/Dropout/Gradient clipping/Scheduler	none

test accuracy at the epoch achieving the best validation accuracy. Results are averaged over 7 seeds. Table 3 summarizes our training implementation. During training, some runs failed; therefore, we introduce an additional rule to handle these cases (see Appendix D.1).

Training-time augmentations are identical across all methods: SO(3) rotation, permutation, and jitter with standard deviation σ_{jitter} . We choose σ_{jitter} based on the noise level of each dataset: $\sigma_{jitter} = 0.02$ for ModelNet/ShapeNet and $\sigma_{jitter} = 0.01$ for SUO. Unless noted otherwise, we set $\Theta = 1.7$, the block repetition $B = 12$, and use aggregation {mean, max, var, min, std, sum}. For neighborhood-based baselines (PointMLP, PointTransformer, DGCNN), we use $k \in \{1, 2, 3\}$ when $N \in \{4, 5, 6\}$. More details of the implementation are available at github.com/YonseiQC/equivariant_QML.

C.3. Baseline Architectures

This appendix details how we instantiate the Light and Mid variants for each baseline family. We follow a simple rule: scale widths and, where explicitly stated, the number of repeated blocks until the target parameter count is reached, while avoiding structural omissions. In particular, we keep all architectural components of the original backbones (e.g., pooling operators, neighborhood definitions, positional-encoding schemes), except for operations that become ill-defined or redundant at our tiny point budgets (such as internal resampling layers); only layer widths (and the number of block repetitions, when noted) are reduced. For each family below, we briefly describe the original model, and the concrete width/depth settings for the Light/Mid variants are summarized next to the comparison tables in this appendix (see Tables 4, 5, 6, 7, 8, 9 and 10).

MLP. A plain fully connected network that consumes flattened coordinates in \mathbb{R}^{3N} . The vector is processed by a stack of dense layers with tanh activations, followed by a linear classifier. No permutational-equivariant structure, attention, or graph operations are used; geometry is inferred from the raw coordinate vector. Depth/width are scaled only to satisfy the Light/Mid capacity targets.

Set-MLP. A shared per-point MLP maps $x_i \in \mathbb{R}^3$ to \mathbb{R}^d , followed by a symmetric aggregation (e.g., mean, max, or standard-deviation pooling) and a small fully connected head, so that the resulting set representation is permutation-invariant with respect to the input point order. Light/Mid variants reduce the per-point tower and head widths while maintaining the aggregation and normalization of the original.

PointNet (Qi et al., 2017a). Our PointNet backbone follows the original design with input and feature transform networks (T-Nets) and a global set pooling stage. An input T-Net first predicts a 3×3 affine transform that is applied to the raw coordinates $x_i \in \mathbb{R}^3$, roughly canonicalizing the point cloud and improving robustness to rigid transforms such as rotations; a shared per-point MLP then maps the transformed points to higher-dimensional features. A second feature T-Net predicts a feature-space transform that is applied before another shared MLP tower. The resulting per-point features are aggregated into a global shape descriptor via symmetric max pooling over the point dimension, and a shallow MLP classifier head maps this global feature to logits, yielding a permutation-invariant set representation.

For the Light/Mid variants, we uniformly narrow the widths of the per-point MLP towers and the classifier head, and

proportionally scale down the T-Net MLPs to meet the $\sim 1.5K$ and $\sim 7K$ parameter budgets, while keeping the input-transform \rightarrow per-point MLP \rightarrow feature-transform \rightarrow global max-pooling \rightarrow classifier-head computation pattern identical to the original. Concrete width/depth configurations for all Light/Mid variants are summarized in the PointNet family tables in this appendix (see Table 4).

DGCNN (Wang et al., 2019). Our DGCNN backbone follows the original dynamic-graph design: at each EdgeConv stage, a k -NN graph is constructed in the current feature space, and edge features are formed by concatenating central-node and offset features (e.g., $[h_i \parallel h_j - h_i]$) over neighbors $j \in \mathcal{N}(i)$. A shared MLP is applied to these edge features and aggregated over neighbors (typically by max pooling) to produce updated point features, and the k -NN graph is recomputed on the new features before the next EdgeConv stage. After repeating these steps multiple times, we concatenate or stack multiscale point features, apply a global symmetric pooling over the point dimension to obtain a shape-level descriptor, and pass it through a shallow MLP classifier head, yielding a permutation-invariant set representation.

For the Light/Mid variants, we preserve dynamic k -NN graph updates, the EdgeConv formulation, and we only scale down channel widths in the EdgeConv MLPs and classifier head; when necessary to meet the $\sim 1.5K$ and $\sim 7K$ parameter budgets, we also reduce the number of EdgeConv stages while keeping the overall dynamic-graph \rightarrow EdgeConv \rightarrow global pooling \rightarrow classifier-head computation pattern unchanged. Concrete width/depth configurations for all Light/Mid variants are summarized in the DGCNN family tables in this appendix (see Table 5).

PointTransformer (Zhao et al., 2021). The original PointTransformer backbone first projects input features to a 32-dimensional latent space and then applies a stack of point-transformer blocks that perform self-attention over local k -NN. Trainable relative positional encodings $\delta(p_i - p_j)$ are injected into both the attention generation branch and the feature transformation branch. Feature widths increase through multiple stages with hierarchical downsampling (e.g., FPS), followed by global average pooling and a fully connected classifier head.

For the Light/Mid variants, we keep the explicit input projection, the relative positional-encoding scheme, vector attention method, FFN block structure and residual connections, but remove the multiscale hierarchy and any FPS-style resampling; a fixed small k -NN graph (defined in coordinate space) is used on the full point set (recomputed per block for simplicity but effectively identical for a given input), and two compact point-transformer blocks operate at reduced widths (tens of channels rather than hundreds). A lightweight Conv1d classifier head maps the final per-point features to logits and then averages over points, yielding a permutation-invariant prediction. All modifications are implemented by shrinking the projection and block widths (and, where necessary, the number of blocks) to meet the $\sim 1.5K$ and $\sim 7K$ parameter budgets, with concrete configurations summarized in the Point Transformer family table (Table 6).

PointMLP (Ma et al., 2022). Our PointMLP backbone follows the residual MLP framework of Ma et al.: given an input point cloud, it progressively extracts local features over a sequence of stages built on k -NN. At each stage, a lightweight geometric affine module first transforms local point coordinates/features within each neighborhood, after which residual per-point MLP (ResP) blocks process per-point features before and after a simple k -NN-based local aggregation. Between stages, the network performs point downsampling to gradually increase the receptive field and reduce the number of points. After the final stage, per-point features are aggregated by a global symmetric pooling over the remaining points to produce a shape-level descriptor, which is fed into a shallow MLP classifier head to output logits.

For the Light/Mid variants, we simplify the original hierarchical architecture to suit our experimental setting: We remove FPS-based resampling and have the network operate at a single resolution, using only k -NN to build local neighborhoods in the initial Geometric Affine encoder. We preserve the residual point-MLP block structure and the geometric affine/context-fusion design, but uniformly scale down channel widths in the stem, stages, and classifier head to meet the $\sim 1.5K$ and $\sim 7K$ parameter budgets; when necessary, we also shorten the number of stages. Global features are obtained by max pooling over all N points. Concrete width/depth configurations for our Light/Mid PointMLP baselines are summarized in the PointMLP family tables in this appendix (see Table 7).

PointMamba (Liang et al., 2024). The original PointMamba backbone converts the unordered 3D point set into a 1D token sequence using a space-filling-curve (SFC) based tokenizer. Starting from the raw point cloud, it selects a subset of points as centers via farthest-point sampling (FPS) and serializes these centers using fixed SFC scans (e.g., Hilbert and Trans-Hilbert). For each serialized center, it forms a local patch via k -NN and applies a lightweight PointNet-style MLP to aggregate patch points into a patch token. To distinguish tokens from different scans, a learnable order indicator

(e.g., per-scan scale/shift) is added, and the two token sequences are concatenated and fed into stacked Mamba blocks. This sequence is processed by a stack of Mamba state-space blocks that apply selective 1D sequence modeling: each block uses pre-LayerNorm, a linear projection into two branches, a depthwise 1D convolution for local mixing, and an input-conditioned selective SSM recurrence parameterized by $A, B, C, \Delta t, D$, followed by a gated output and residual connection. Finally, a global pooling plus linear classifier maps the final sequence features to class logits.

For the Light/Mid variants, we retain the selective Mamba block structure, and a pooling head, but substantially reduce the model depth and channel widths. We keep the SFC-style point-to-sequence serialization based on Hilbert/Trans-Hilbert scans, but in the sparse-point regime, we directly tokenize each point and omit any FPS- or k -NN-based grouping (patching) altogether (compared to architectures that rely on k -NN as a core inductive bias, PointMamba does not inherently require them). To ensure a uniform implementation environment across all baselines, we do not rely on the official `mamba-ssm` library. Instead, we implement our own compact Mamba block in plain PyTorch that follows the same selective state-space formulation, but forgoes the fused CUDA kernels and other low-level optimizations of the original implementation. All modifications are realized by shrinking the embedding, state, and block widths (and, where needed, the number of blocks) to fit the $\sim 1.5K$ and $\sim 7K$ parameter budgets, with concrete Light/Mid configurations summarized in the PointMamba family table (Table 8).

Mamba3D (Han et al., 2024). The original Mamba3D backbone is built around two key components—a local norm pooling (LNP) and a bidirectional state-space module (bi-SSM) tailored for 3D point clouds. Given an unordered point set in \mathbb{R}^3 , Mamba3D first applies FPS & k -NN and obtains initial patch tokens via a lightweight PointNet-style embedding. The LNP block then aggregates local context over token neighborhoods via k -norm propagation and k -pooling (with a shared MLP for channel alignment). This sequence is subsequently processed by a bi-SSM block, which applies a Mamba-style selective state-space model along the token dimension (L+SSM) and a second selective SSM along the feature-channel dimension (C-SSM) using a channel flip, and fuses both directions through residual connections followed by a classification head.

For the Light/Mid variants, we retain the LNP token-mixing and bi-SSM channel-mixing blocks, including the feature-channel flip for C-SSM, along with the original pre-norm residual block structure and positional encoding injected at each encoder layer. However, since our evaluation focuses on extremely small point regimes, we omit the FPS- and k -NN-based patch construction (compared to architectures that rely on k -NN as a core inductive bias, Mamba3D does not inherently require them) and instead operate directly on per-point tokens (with LNP applied over a global token neighborhood). To ensure a uniform implementation environment across all baselines, we do not rely on the original Mamba3D codebase or the official `mamba-ssm` library. While the reference Mamba3D implementation builds its bidirectional C-SSM core using the Mamba selective state-space module from `mamba-ssm`, our Light/Mid variants replace this component with a custom PyTorch implementation of the same selective state-space update with the feature-channel flip used for C-SSM. The resulting compact backbone is mathematically consistent with the original formulation but omits fused CUDA kernels and other low-level engineering optimizations. All modifications are realized by shrinking the embedding, state, and block widths (and, where needed, the number of blocks) to fit the $\sim 1.5K$ and $\sim 7K$ parameter budgets, with concrete Light/Mid configurations summarized in the Mamba3D family table (Table 9).

RP-EQGNN (Liu et al., 2025). RP-EQGNN is a quantum graph neural network that exploits rotational and permutational symmetries for 3D graph data. In the paper, the model is organized into three quantum modules: (i) The rotation- and permutation-equivariant module U_R comprises a geometric information encoding circuit U_φ and a geometric information entanglement circuit U_ϕ , where U_φ encodes node coordinates using universal rotation gates, mapping them into a Hilbert space while U_ϕ entangles qubits to learn geometric relations. (ii) The convolution and entanglement module U_N consists of a non-geometric information convolution circuit U_C and a non-geometric information entanglement circuit U_E , and is responsible for extracting node features. (iii) A geometric de-entanglement module U_R^\dagger is applied to preserve equivariance, after which the model output is produced via measurement and followed by classical post-processing for prediction.

However, the description of RP-EQGNN within the original paper cannot produce simultaneously rotation- and permutation-invariant outputs for mathematical reasons. To obtain an invariant output within their framework, the model would require an $SU(2)$ -invariant initial state and Hamiltonian, and an $SU(2)$ -commuting encoding gate. However, they initialize the state as $|0\rangle$, which is not $SU(2)$ -invariant, and the paper provides no details on the specific Hamiltonian or the construction of the encoding gate. On the other hand, in the official implementation from GitHub¹, they use a Pauli- Z Hamiltonian and a direct

¹https://github.com/wqs1999/RP-EQGNN_YiFanZhu (commit da7cba0, accessed on 2025-12-31).

coordinate encoding, which does not ensure the $SU(2)$ invariance.

For the Light/Mid variants, we inspected the authors' official public implementation. We found that the released code does not provide a one-to-one realization of the above modular decomposition. Specifically, the implementation consists of (i) coordinate encoding, (ii) node-feature encoding, and (iii) edge-conditioned entanglement, without the full structure described in the paper. Moreover, the released implementation is evaluated only on QM9, rather than on point cloud classification benchmarks. Therefore, in our baseline, we implement a compact RP-EQGNN circuit that follows the overall design of the official implementation, while adapting the feature definitions to our point cloud setting. For node-feature encoding, we apply single-qubit RY and RX rotations parameterized by a scalar node feature defined as the point norm. For edge-conditioned entanglement, we use the pairwise distance between two points and the angle between their position vectors (with respect to the origin) as edge features. The resulting architectural differences from the official implementation and our concrete Light/Mid configurations are summarized in Table 10.

Table 4. PointNet family: Original vs. Light vs. Mid.

Component	PointNet_Original	PointNet_Light	PointNet_Mid
Input T-Net (3×3)	$3 \rightarrow 64 \rightarrow 128 \rightarrow 1024$	$3 \rightarrow 8 \rightarrow 10$	$3 \rightarrow 8 \rightarrow 10$
Per-point stem	$3 \rightarrow 64 \rightarrow 64$	$3 \rightarrow 9$	$3 \rightarrow 4 \rightarrow 8$
Feature T-Net ($k \times k$)	$64 \rightarrow 64 \rightarrow 128 \rightarrow 1024 \rightarrow k^2 (k=64)$	$9 \rightarrow 9 \rightarrow 10 \rightarrow k^2 (k=9)$	$8 \rightarrow 16 \rightarrow 20 \rightarrow k^2 (k=8)$
Feature blocks (per-point)	$64 \rightarrow 64 \rightarrow 128 \rightarrow 1024$	(none)	$8 \rightarrow 32 \rightarrow 120 \rightarrow 8$
Pooling	$\rightarrow 1024$	$\rightarrow 9$	$\rightarrow 8$
Classifier / Head	$1024 \rightarrow 512 \rightarrow 256 \rightarrow K + \text{Dropout}(0.3)$	$9 \rightarrow 16 \rightarrow K$ (no dropout)	$8 \rightarrow K$ (no dropout)
Activation / Normalization	ReLU + BatchNorm	ReLU + BatchNorm	ReLU + BatchNorm
Structural differences	Baseline	T-Nets/feature blocks present (reduced); head reduced	T-Nets/feature blocks present (reduced); head reduced

Table 5. DGCNN family: Original vs. Light vs. Mid.

Component	DGCNN_Original	DGCNN_Light	DGCNN_Mid
Input Encoding	Edge feature MLPs in EdgeConv, from $(p_i, p_j, p_i - p_j) \rightarrow 64$	Edge feature MLPs with narrow channel width ($6 \rightarrow 7$); we use the same formulation, but with edge features $(p_j - p_i, p_i)$ instead of $(p_i, p_j, p_i - p_j)$.	Same as light, but with a narrow edge feature MLP mapping ($6 \rightarrow 8$).
Positional Encoding	No explicit PE; uses relative offsets $p_i - p_j$ within EdgeConv	No explicit PE; relative offsets used implicitly (same)	No explicit PE; relative offsets used implicitly (same)
Stem / Input Embedding	EdgeConv-1: dynamic k -NN graph, $6 \rightarrow 64$	EdgeConv-1: dynamic k -NN graph, $6 \rightarrow 7$	EdgeConv-1: dynamic k -NN graph, $6 \rightarrow 8$
Feature Blocks and Depth	EdgeConv-2: $2 \times 64 \rightarrow 64$; EdgeConv-3: $2 \times 64 \rightarrow 128$; EdgeConv-4: $2 \times 128 \rightarrow 256$	EdgeConv-2: $2 \times 7 \rightarrow 15$; EdgeConv-3: $2 \times 15 \rightarrow 8$	EdgeConv-2: $2 \times 8 \rightarrow 32$; EdgeConv-3: $2 \times 32 \rightarrow 72$
Sampling / Grouping	k -NN with dynamic graph (per layer); no FPS	k -NN with dynamic graph; no FPS	k -NN with dynamic graph; no FPS
Pooling	Global max pooling over concatenated multiscale edge features $\rightarrow 512$	Global max pooling $\rightarrow 30$	Global max pooling $\rightarrow 112$
Classifier / Head	Fully connected $512 \rightarrow 256 \rightarrow K$	Fully connected $30 \rightarrow 13 \rightarrow 9 \rightarrow K$	Fully connected $112 \rightarrow 16 \rightarrow 9 \rightarrow K$
Activation / Normalization	Leaky ReLU + BatchNorm	Leaky ReLU + BatchNorm	Leaky ReLU + BatchNorm
Structural Differences	Four EdgeConv stages; sometimes extra 1×1 conv $\rightarrow 1024$ before pooling	Fewer stages; narrower channels; no extra 1×1 conv before pooling	Fewer stages; narrower channels; no extra 1×1 conv before pooling

Table 6. PointTransformer family: Original vs. Light vs. Mid.

Component	PointTransformer_Original	PointTransformer_Light	PointTransformer_Mid
Input Encoding	Linear/Conv1d $C_{in} \rightarrow 32$ before Block 1	Linear/Conv1d $C_{in} \rightarrow 5$ before Block 1	Linear/Conv1d $C_{in} \rightarrow 8$ before Block 1
Positional Encoding	Relative PE $\delta(p_i - p_j)$ via small MLP; added to attention and feature bias	Relative PE retained; no learned absolute PE	Relative PE retained; no learned absolute PE
Input Embedding	Block 1: Transformer block on 32-d features	Block 1: Transformer block on 5-d features	Block 1: Transformer block on 8-d features
Feature Blocks and Depth	Blocks: 32 (B1) \rightarrow 64 (B2) \rightarrow 128 (B3) \rightarrow 256 (B4) \rightarrow 512 (B5)	Blocks: 5 (B1) \rightarrow 7 (B2) \rightarrow 8	Blocks: 8 (B1) \rightarrow 14 (B2) \rightarrow 18
Transformer Block	Block 1: 32 \rightarrow 32; Attn: 32 \rightarrow 32; Linear: 32 \rightarrow 32; Residual $\times 1$ Block 2: 64 \rightarrow 64; Attn: 64 \rightarrow 64; Linear: 64 \rightarrow 64; Residual $\times 1$ Block 3: 128 \rightarrow 128; Attn: 128 \rightarrow 128; Linear: 128 \rightarrow 128; Residual $\times 1$ Block 4: 256 \rightarrow 256; Attn: 256 \rightarrow 256; Linear: 256 \rightarrow 256; Residual $\times 1$ Block 5: 512 \rightarrow 512; Attn: 512 \rightarrow 512; Linear: 512 \rightarrow 512; Residual $\times 1$	Block 1: 5 \rightarrow 7; Attn: 7 \rightarrow 7; Linear: 7 \rightarrow 28 \rightarrow 7; Residual $\times 2$ Block 2: 7 \rightarrow 8; Attn: 8 \rightarrow 8; Linear: 8 \rightarrow 32 \rightarrow 8; Residual $\times 2$	Block 1: 8 \rightarrow 14; Attn: 14 \rightarrow 14; Linear: 14 \rightarrow 56 \rightarrow 14; Residual $\times 2$ Block 2: 14 \rightarrow 18; Attn: 18 \rightarrow 18; Linear: 18 \rightarrow 72 \rightarrow 18; Residual $\times 2$
Sampling / Grouping	Hierarchical downsampling (e.g., FPS); local k -NN	No hierarchical downsampling; fixed small k -NN on full set	No hierarchical downsampling; fixed small k -NN on full set
Classifier / Head	The paper does not provide classifier-layer details, and we could not verify an official classification implementation	Conv1d 8 \rightarrow 8 \rightarrow K ; then mean over points	Conv1d 18 \rightarrow 18 \rightarrow K ; then mean over points
Activation / Normalization	The paper does not provide classifier-layer details, and we could not verify an official classification implementation	ReLU + LayerNorm	ReLU + LayerNorm
Structural Differences	Full multiscale hierarchy; explicit input projection; relative PE	Removes hierarchy; keeps explicit input projection and relative PE	Removes hierarchy; keeps explicit input projection and relative PE

Table 7. PointMLP Family.

Component	PointMLP(elite)_Original	PointMLP_Light	PointMLP_Mid
ResidualMLPBlock	Two FC–BN–Act; skip projection if in=out	Two FC–BN–Act; skip proj if in=out	Two FC–BN–Act; skip proj if in=out
PointMLPStage	Pre residual (in→in); Grouping + local MLP; Post residual (in→out)	Pre residual(in→in); Aggregation + MLP (no grouping); Post residual(in→out)	Pre residual(in→in); Aggregation + MLP (no grouping); Post residual(in→out)
Stem / Input	Linear 3 → 32; BN+ReLU	Linear 3 → 6; BN+ReLU	Linear 3 → 8; BN+ReLU
Stage 1	32 → 64	6 → 10	8 → 8
Stage 2	64 → 128	10 → 12	8 → 16
Stage 3	128 → 256	—	16 → 32
Stage 4	256 → 256	—	—
Encoding	Stage-wise encoders with FPS+ k -NN; per-stage outputs: 32 → 64, 64 → 128, 128 → 256, 256 → 256 with down sampling	Once (outside stages): GAEncode with k -NN; 6 → 6 (no down sampling)	Once (outside stages): GAEncode with k -NN; 8 → 8 (no down sampling)
Pooling	Max over 64 sampled points → 256	Max → 12	Max → 32
Classifier / Head	256 → 512 → 256 → K	12 → 8 → K	32 → 16 → 8 → K
Activation / Normalization	ReLU + BatchNorm	ReLU + BatchNorm	ReLU + BatchNorm
Structural differences	Full hierarchy (4 stages), resampling enabled	Hierarchy removed; widths reduced; single-scale	Hierarchy removed; widths reduced; single-scale

Table 8. PointMamba family: Original vs. Light vs. Mid.

Component	PointMamba_Original	PointMamba_Light	PointMamba_Mid
Input Encoding / Tokens	Point cloud is partitioned into local point patches by FPS+ k -NN; each patch is converted to relative coordinates and encoded by a PointNet-style MLP into a 384-dimensional patch token.	No FPS or k -NN grouping; each 3D point is directly treated as a token and projected by a linear layer $3 \rightarrow 5$, yielding N tokens per traversal (Hilbert/Trans-Hilbert), concatenated to $2N$ tokens width = 5.	Same as Light, a linear point embedding $3 \rightarrow 5$ is used, producing $2N$ tokens.
SFC Ordering & Order Indicator	Two space-filling curves (Hilbert and Trans-Hilbert) and a learnable order-indicator module with per-order scale-shift parameters (γ, β) are applied to input tokens and the two traversals are concatenated into a single sequence.	Uses exactly the same pair of SFC traversals and the same order-indicator mechanism (γ, β) as the original.	Same SFC ordering and order-indicator mechanism as Light.
Mamba Blocks (Depth & Width)	Vanilla Mamba encoder with 12 Mamba blocks; each block operates on 384-dimensional tokens.	Four compact Mamba blocks with $d_{\text{model}}=5$, inner width $d_{\text{inner}}=10$ (expand= 2), state size $d_{\text{state}}=6$, and depthwise Conv1d kernel size $d_{\text{conv}}=2$.	Nineteen compact Mamba blocks with $d_{\text{model}}=5$, $d_{\text{inner}}=10$ (expand= 2), $d_{\text{state}}=6$, and depthwise Conv1d kernel size $d_{\text{conv}}=2$.
Selective SSM Implementation	Selective SSM recurrence $(A, B, C, \Delta t, D)$ implemented via the official <code>mamba-ssm</code> library with fused CUDA kernels and other low-level optimizations.	Implements the same selective SSM equations in plain PyTorch (state tensor $B \times d_{\text{inner}} \times d_{\text{state}}$), without fused kernels, targeting simple CPU-friendly execution.	Same PyTorch Mamba implementation as Light; only the dimensionalities $(d_{\text{model}}, d_{\text{inner}}, d_{\text{state}}, d_{\text{conv}})$ differ as above.
Pooling & Classifier Head	Global average pooling over the final token sequence, followed by a single linear classifier $384 \rightarrow K$.	LayerNorm on token features, then mean pooling over all $2N$ tokens, followed by linear classifier $5 \rightarrow K$.	LayerNorm on token features, then mean pooling over all $2N$ tokens, followed by linear classifier $5 \rightarrow K$.
Activation / Normalization	Pre-LayerNorm inside each Mamba block; SiLU activation after the depthwise Conv1d branch; sigmoid gate on the SSM output; residual connection $x+y$.	Uses the same block-level structure as the original (pre-LN, SiLU after Conv1d, sigmoid gate, residual connection).	Same as Light.
Structural Differences	Full-capacity PointMamba encoder over SFC-ordered patch tokens, using the official <code>mamba-ssm</code> kernels.	Operates directly on point tokens (no FPS, k -NN), with drastically reduced widths and depth to fit a ~ 1.5 K-parameter budget and to run with the plain PyTorch Mamba implementation instead of <code>mamba-ssm</code> .	Same tokenizer and PyTorch Mamba design as Light, but deeper settings targeting a ~ 7 K-parameter budget.

Table 9. Mamba3D family: Original vs. Light vs. Mid.

Component	Mamba3D_Original	Mamba3D_Light	Mamba3D_Mid
Input encoding	Patch embeddings via FPS (L centers) + k -NN (k points/patch) + light-PointNet, then add [CLS] and learnable positional encoding to obtain an $L + 1$ token sequence.	Per-point tokenization with a linear point embedding $3 \rightarrow 5$, plus a coordinate-based positional embedding added to each token; prepend a learnable [CLS] token (with its own positional parameter). No FPS/ k -NN patching is used; tokens remain per-point.	Same tokenizer and LNP as Light, with point embedding $3 \rightarrow 5$ and learnable [CLS] token.
bi-SSM & LNP blocks	12-layer encoder at width 384; each layer applies LNP with $k=4$ and a bi-SSM (L+SSM and C-SSM) following the original setting.	Two compact blocks (LNP + bi-SSM). L+SSM uses $(d_{\text{model}}, d_{\text{state}}, d_{\text{conv}}, \text{expand}) = (5, 6, 2, 2)$, while C-SSM uses $(d_{\text{model}}, d_{\text{state}}, d_{\text{conv}}, \text{expand}) = (N + 1, 6, 2, 2)$ (with $N \in \{4, 5, 6\}$); LNP uses a global all-pairs neighborhood.	Eight compact blocks with the same per-block settings as Light: L+SSM $(5, 6, 2, 2)$ and C-SSM $(N + 1, 6, 2, 2)$ (with $N \in \{4, 5, 6\}$); LNP uses a global all-pairs neighborhood.
Selective SSM implementation	Uses the official mamba-ssm selective SSM module with fused CUDA kernels for both L+SSM and C-SSM.	Reimplements the same selective SSM update in pure PyTorch for L+SSM and C-SSM with feature-channel flip; no fused CUDA kernels or low-level optimizations.	Same PyTorch selective SSM implementation as Light; only depth differs.
Pooling & classifier head	Classifies using the final [CLS] token (linear head on [CLS] after the encoder).	LayerNorm + linear classifier $5 \rightarrow K$ on the final [CLS] feature.	Same as Light: LayerNorm + linear classifier $5 \rightarrow K$ on the final [CLS] feature.
Activation / normalization	Layer normalization and SiLU activation inside each Mamba block with sigmoid gating on the SSM output and residual connections.	Same block-level normalization and activations as Original (LayerNorm, SiLU, sigmoid gate, residual).	Same as Light.
Structural differences	Full-capacity Mamba3D encoder on patch tokens, using the official mamba-ssm implementation and original depth/width settings.	Keeps the original LNP+bi-SSM+[CLS] architecture but removes FPS/ k -NN and shrinks embedding, state size and number of blocks to fit a $\sim 1.5K$ parameter budget; uses a compact PyTorch SSM without fused CUDA kernels.	Same architecture as Light, with deeper depth, fitting a $\sim 7K$ parameter budget.

Table 10. RP-EQGNN family: Original vs. Light vs. Mid.

Component	RP-EQGNN_Original	RP-EQGNN_Light	RP-EQGNN_Mid
Coordinate encoder	Geometric information encoding circuit (rotation encoding) maps node coordinates into a Hilbert space (e.g., RY/RX/RY applied to (x, y, z)).	Same as original.	Same as original.
Node-feature encoder	The official implementation uses 11-dimensional per-node input features, injected through a feature-encoding circuit with $4 \times \text{RY} + 7 \times \text{RX}$ rotations per qubit.	Point cloud instantiation: we define a scalar node feature $f_i = \ p_i\ $ and apply RY/RX rotations parameterized by f_i with trainable scaling.	Same as Light, with larger depth.
Edge-conditioned entanglement	Applies edge-conditioned two-qubit entangling gates (RXX), where a 1D scalar edge feature is used per edge to modulate the interaction strength.	Complete-graph entanglement using coordinate-derived edge features: distance $d_{ij} = \ p_i - p_j\ $ and inter-vector angle α_{ij} (w.r.t. the origin) modulate two-qubit interactions (IsingXX).	Same as Light, with larger depth.
Measurement and classical head	Produces outputs via a global symmetric quantum readout, specifically the expectation value of the observable $Z^{\otimes N}$, followed by a small classical post-processing MLP($1 \rightarrow 3 \rightarrow 1$).	Global symmetric readout yielding one scalar quantum feature per sample, followed by an MLP head ($1 \rightarrow 32 \rightarrow 32 \rightarrow K$); uses the same readout observable $Z^{\otimes N}$ as the official implementation.	Same readout; optionally a wider MLP head ($1 \rightarrow 32 \rightarrow 64 \rightarrow 64 \rightarrow 32 \rightarrow K$) under a larger budget.
Structural differences	Evaluated on QM9 and uses graph-provided node/edge attributes in a PyTorch+Qiskit implementation; the coordinate encoder, node-feature encoder, and edge-conditioned entanglement are applied once ($L=1$).	Adapts the official structure to point cloud classification by redefining node/edge features from coordinates, implemented in JAX+PennyLane; the same three components are repeated with depth $L=50$.	Same as Light (JAX+PennyLane) with $L=50$, scaling capacity primarily via depth/width.

Table 11. HyQuRP vs. Set-MLP (Light models).

Component	HyQuRP_Light	Set-MLP_Light
High-level idea	Hybrid quantum-classical model.	Purely classical MLP with pooling, matching the HyQuRP_Light classical part.
Input point shape	Batches of N 3D points $(N, 3)$.	Batches of N 3D points $(N, 3)$.
MLP input representation	Quantum part produces two types of $\binom{N}{2}$ pairwise measurements $(\binom{N}{2}, 2)$.	For comparison with HyQuRP, a neural network transforms $(N, 3) \rightarrow (N, 2)$
Per-point / token MLP	MyNN: shared $2 \rightarrow 4 \rightarrow 4$ MLP (with tanh) on each Hamiltonian feature token.	SimpleNN: shared $2 \rightarrow 4 \rightarrow 4$ MLP (with tanh) on each per-point feature token.
Pooling	Stats over $\binom{N}{2}$ tokens (mean / max / min / sum / std / var) on 4-d features $\rightarrow 24$ -d vector.	Same symmetric stats over N tokens on 4-d features $\rightarrow 24$ -d vector.
Classifier / head	$24 \rightarrow 24 \rightarrow 24 \rightarrow K$ MLP (with tanh) on the global descriptor.	Same $24 \rightarrow 24 \rightarrow 24 \rightarrow K$ MLP (with tanh) head as HyQuRP_Light.
Explicit symmetry handling	Permutation and rotation invariant.	Only permutation invariance from symmetric pooling.

Table 12. HyQuRP vs. Set-MLP (Mid models).

Component	HyQuRP_Mid	Set-MLP_Mid
High-level idea	Same hybrid design as Light, but with a wider classical head for more capacity.	Purely classical MLP with pooling, matching the HyQuRP_Mid classical part.
Input point shape	Same as HyQuRP_Light: Batches of N 3D points $(N, 3)$.	Same as Set-MLP_Light: Batches of N 3D points $(N, 3)$.
MLP input representation	Same as HyQuRP_Light.	Same as Set-MLP_Light.
Per-point / token MLP	MyNN: shared $2 \rightarrow 8 \rightarrow 16 \rightarrow 32$ MLP (with tanh); higher per-token capacity.	SimpleNN: shared $2 \rightarrow 8 \rightarrow 16 \rightarrow 32$ MLP (with tanh); higher per-token capacity.
Pooling	Stats over $\binom{N}{2}$ tokens on 32-d features $\rightarrow 192$ -d vector.	Same stats over N tokens on 32-d features $\rightarrow 192$ -d vector.
Classifier / head	$192 \rightarrow 32 \rightarrow 16 \rightarrow 8 \rightarrow K$ MLP (with tanh) on the global descriptor.	$192 \rightarrow 32 \rightarrow 16 \rightarrow 8 \rightarrow K$ MLP (with tanh) head, deeper and wider.
Explicit symmetry handling	Same as HyQuRP_Light.	Same as Set-MLP_Light.

D. Additional Details

D.1. Details of summary metrics

We follow the reporting convention in Fig. 2 and specify the exact aggregation rules used to compute $\pm\sigma$ and the average rank. σ denotes the sample standard deviation across seeds, computed with Bessel's correction (division by $S - 1$), where $S = 7$. There were a small number of failed runs (16 out of 1,260) where the training loss did not decrease, likely due to loose hyperparameter tuning and instability of neighborhood construction in the sparse-point regime. For these runs, we retried training with the adjacent learning rates on the predefined grid $\{10^{-1}, 10^{-2}, 10^{-3}, 10^{-4}, 10^{-5}\}$, using the lower neighbor first and the higher neighbor second. With this fixed rule, we observed no further failures. For each setting (dataset, point budget, capacity), we rank models by the mean test accuracy; ties are broken by smaller standard deviation. We then average the ranks across all settings.

D.2. Definitions of the cosine similarity and ℓ_2 -norm ratio

Let $z, z' \in \mathbb{R}^C$ denote the logit vectors produced by the same model for an input x and its transformed version $g \cdot x$ (e.g., rotation/permuation), respectively. We define:

$$s_{\text{cosine}}(z, z') := \frac{z^\top z'}{\|z\|_2 \|z'\|_2}. \quad (136)$$

$$s_{\text{norm}}(z, z') := \frac{\|z'\|_2}{\|z\|_2}, \quad (137)$$

$s_{\text{norm}}(z, z')$ can be greater than 1.